

DOCKETED

Docket Number:	07-AFC-05C
Project Title:	Ivanpah Solar Electric Generating System (Compliance)
TN #:	227847
Document Title:	Tools to Address Glare and Avian Flux Hazards from Solar Energy Systems
Description:	N/A
Filer:	Joe Douglas
Organization:	California Energy Commission
Submitter Role:	Energy Commission
Submission Date:	4/24/2019 7:35:24 AM
Docketed Date:	4/24/2019

SANDIA REPORT

SAND2018-10983

Unlimited Release

Printed September 2018

Tools to Address Glare and Avian Flux Hazards from Solar Energy Systems

Clifford K. Ho, Cianan A. Sims, Julius E. Yellowhair, and Timothy Wendelin

Prepared by
Sandia National Laboratories
Albuquerque, New Mexico 87185 and Livermore, California 94550

Sandia National Laboratories is a multimission laboratory managed and operated by National Technology and Engineering Solutions of Sandia, LLC, a wholly owned subsidiary of Honeywell International, Inc., for the U.S. Department of Energy's National Nuclear Security Administration under contract DE-NA0003525.



Sandia National Laboratories

Issued by Sandia National Laboratories, operated for the United States Department of Energy by National Technology and Engineering Solutions of Sandia, LLC.

NOTICE: This report was prepared as an account of work sponsored by an agency of the United States Government. Neither the United States Government, nor any agency thereof, nor any of their employees, nor any of their contractors, subcontractors, or their employees, make any warranty, express or implied, or assume any legal liability or responsibility for the accuracy, completeness, or usefulness of any information, apparatus, product, or process disclosed, or represent that its use would not infringe privately owned rights. Reference herein to any specific commercial product, process, or service by trade name, trademark, manufacturer, or otherwise, does not necessarily constitute or imply its endorsement, recommendation, or favoring by the United States Government, any agency thereof, or any of their contractors or subcontractors. The views and opinions expressed herein do not necessarily state or reflect those of the United States Government, any agency thereof, or any of their contractors.

Printed in the United States of America. This report has been reproduced directly from the best available copy.

Available to DOE and DOE contractors from
U.S. Department of Energy
Office of Scientific and Technical Information
P.O. Box 62
Oak Ridge, TN 37831

Telephone: (865) 576-8401
Facsimile: (865) 576-5728
E-Mail: reports@osti.gov
Online ordering: <http://www.osti.gov/scitech>

Available to the public from
U.S. Department of Commerce
National Technical Information Service
5301 Shawnee Rd
Alexandria, VA 22312

Telephone: (800) 553-6847
Facsimile: (703) 605-6900
E-Mail: orders@ntis.gov
Online order: <http://www.ntis.gov/search>



Tools to Address Glare and Avian Flux Hazards from Solar Energy Systems

Clifford K. Ho,¹ Cianan A. Sims,² Julius E. Yellowhair,¹ and Timothy Wendelin³

¹Org. 08823 Concentrating Solar Technologies, Sandia National Laboratories, P. O. Box 5800, Albuquerque, NM 87185-1127

²Sims Industries, 6077 Far Hills Ave #101, Centerville, OH 45459

³National Renewable Energy Laboratory, 15013 Denver W Pkwy, Golden, CO 80401 (retired)

Abstract

This report describes software tools that can be used to evaluate and mitigate potential glare and avian-flux hazards from photovoltaic and concentrating solar power (CSP) plants. Enhancements to the Solar Glare Hazard Analysis Tool (SGHAT) include new block-space receptor models, integration of PVWatts for energy prediction, and a 3D daily glare visualization feature. Tools and methods to evaluate avian-flux hazards at CSP plants with large heliostat fields are also discussed. Alternative heliostat standby aiming strategies were investigated to reduce the avian-flux hazard and minimize impacts to operational performance. Finally, helicopter flyovers were conducted at the National Solar Thermal Test Facility and at the Ivanpah Solar Electric Generating System to evaluate the alternative heliostat aiming strategies and to provide a basis for model validation. Results showed that the models generally overpredicted the measured results, but they were able to simulate the trends in irradiance values with distance. A heliostat up-aiming strategy is recommended to alleviate both glare and avian-flux hazards, but operational schemes are required to reduce the impact on heliostat slew times and plant performance. Future studies should consider the trade-offs and collective impacts on these three factors of glare, avian-flux hazards, and plant operations and performance.

ACKNOWLEDGMENTS

The authors thank Chris Nichols and Michele Boyd for their support and management of this work. This work was funded by the U.S. Department of Energy's Solar Energy Technologies Office (Soft Costs project 1535). Sandia National Laboratories is a multimission laboratory managed and operated by National Technology and Engineering Solutions of Sandia, LLC., a wholly owned subsidiary of Honeywell International, Inc., for the U.S. Department of Energy's National Nuclear Security Administration under contract DE-NA0003525.

TABLE OF CONTENTS

1.	Introduction.....	9
	1.1. Background and Problem Statement.....	9
	1.2. Objectives	10
2.	Solar Glare Hazards and Analyses.....	10
	2.1. Glare Hazards.....	10
	2.2. Glare Tools.....	12
	2.2.1. Solar Glare Hazard Analysis Tool (SGHAT)	12
	2.2.2. ForgeSolar	16
	2.2.3. SolTrace and SolarPILOT	17
	2.2.4. Tower Illuminance Model (TIM).....	17
	2.3. Glare Technical Assistance and Outreach	19
	2.4. Summary	22
3.	Solar Flux Hazards and Analyses	22
	3.1. Introduction to Avian Flux Hazards	22
	3.2. Modeling Approaches to Evaluate Avian Flux Hazards.....	23
	3.2.1. Energy Balance and Bird Feather Heating.....	23
	3.2.2. Evaluation of Alternative Heliostat Standby Aiming Strategies.....	28
	3.2.3. Heliostat Slew Times and Annual Performance	30
	3.3. Results.....	31
	3.3.1. Flux Maps	31
	3.3.2. Avian Flux Hazard and Impact on Annual Operating Performance	33
	3.3.3. Summary	36
4.	Validation Studies.....	37
	4.1. Helicopter Flyover of NSTTF.....	37
	4.2. Helicopter Flyover of Ivanpah Solar Electric Generating System.....	43
	4.2.1. Summary of Previous and Current Flyovers	44
	4.2.2. Evaluation of Current Flyover of Ivanpah	46
	4.3. Summary	52
5.	Conclusions.....	53
	5.1. Glare Hazard Analyses	53
	5.2. Flux Hazard Analyses	53
	5.3. Validation.....	53
	5.4. Recommendations.....	54
	Appendix A – Validation of Block Space Receptor Feature in SGHAT	59

FIGURES

Figure 1. Examples of solar glare. Left: PV system at Manchester-Boston Regional Airport viewed from the air-traffic control tower. Right: Glare from Ivanpah CSP plant viewed from an aircraft.	9
Figure 2. Potential ocular impacts of retinal irradiance as a function of subtended source angle [29]. Note: 1 watt yields approximately 100 lumens of visible light in the solar spectrum.	11
Figure 3. Illustration of specular and diffuse reflections.	12
Figure 4. Screen image of SGHAT with Google Map interface and interactive drawing tools to prescribe the location of the PV array (blue outline) and observation points (red marker).	13
Figure 5. Block space analysis concept. User outlines entire region, such as airport airspace, rather than discrete points.	14
Figure 6. Validation of PVWatts vs. SGHAT, adjusted for weather.	15
Figure 7. Glare Visualization of MHT array (purple) with Air Traffic Control Tower (white), flight path (green), and cumulative daily glare for July 1.	16
Figure 8. ForgeSolar website (https://forgesolar.com).	16
Figure 9. Top: Screen image from TIM software tool. Bottom: Ocular hazard data along a vertical cross-section (green=low potential for ocular impact; yellow= potential for temporary after-image).	18
Figure 10. Number of registrations for SGHAT or ForgeSolar tools by quarter.	21
Figure 11. Total PV rated capacity (MW) analyzed using SGHAT technology.	22
Figure 12. Left: Illuminated standby aim points next to the receiver at Ivanpah using original aim-point strategy before changes were made. Right: MacGillivray Warbler with “Grade 3” solar flux injury found at Ivanpah [19].	23
Figure 13. Energy balance on control volume of feather barb exposed to solar irradiance.	24
Figure 14. Illustration of the illuminated air space above the heliostat field at Ivanpah and bird flight paths.	27
Figure 15. Sample of flight paths superimposed on plan view of simulated flux map over Ivanpah Unit 2.	28
Figure 16. Dimensions used to calculate safe distance above receiver for a single point-focus aim point directly above the receiver.	30
Figure 17. Impact of startup time on annual energy production normalized to 30-minute startup time.	31
Figure 18. Flux maps at three different elevations (80, 122 (receiver midplane), and 160 m) for three heliostat standby aiming strategies (Baseline, Option 3, and Option 6) at solar noon on the summer solstice.	32
Figure 19. Flux maps at different elevations with all standby heliostats aimed at a single point 20 m above the top of the receiver (160 m elevation) at solar noon, summer solstice.	33
Figure 20. Example of modeled bird-feather temperatures along a single flight path (flying from north to south) along a horizontal transect (Option 3, 122 m elevation).	34
Figure 21. Plot of normalized performance metrics as a function of radial extent of aim points.	36
Figure 22. Helicopter flyover of the NSTTF. Left: Julius Yellowhair (Sandia), Cliff Ho (Sandia), and Shawn Mease (Mountain Air Helicopters). Right: Ready for takeoff.	38

Figure 23. Left: Route from Mountain Air Helicopters in Los Lunas to the NSTTF on KAFB. Right: locations of photographs for irradiance calculations at altitudes from ~1000 feet to ~4000 feet above ground level.	38
Figure 24. Views of glare at short, medium, and long observation distances using a single aimpoint strategy (20 m to the east (right) and 20 m above the top of the tower). .	39
Figure 25. Views of glare at short, medium, and long observation distances using a dual aimpoint strategy (20 m to the west and east of the top of the tower and 20 m above).	39
Figure 26. Views of conventional standby aiming (dual aimpoint) (left) and up-aiming strategy (right).	40
Figure 27. TIM simulations of glare from the NSTTF (single aimpoint) at the short, medium, and long observation distances.	41
Figure 28. SolTrace simulation of a single aimpoint strategy at the NSTTF.	42
Figure 29. Measured and predicted corneal irradiance as a function of distance to glare source at the NSTTF.	42
Figure 30. Parity plot of simulated irradiance vs. measured irradiance at the NSTTF.	43
Figure 31. Filtered images of heliostat glare showing reflections from individual facets.	43
Figure 32. Sequence of photos of glare at Ivanpah taken on different dates looking northwest. Note that on May 24, 2018, Unit 1 was not operational.	46
Figure 33. From left to right: Carl Maassberg (NRG), Cliff Ho (Sandia), and Mike Toland (Mission Support & Test Services, Nellis AFB) prior to flyover of Ivanpah on May 24, 2018.	47
Figure 34. Locations of photographs taken on May 24, 2018.	47
Figure 35. Left: Looking northwest at Units 2 and 3. Right: Looking southeast at Units 3, 2, and 1 (Unit 1 was not operational).	48
Figure 36. Photos of glare at Ivanpah (top) and filtered images (bottom) revealing glare from individual facets. The intensity of the glare was notably less than previous flyovers.	49
Figure 37. Simulations of irradiance at Ivanpah (Unit 2) using SolTrace (top) and TIM (bottom).	50
Figure 38. Measured and predicted corneal irradiance as a function of distance to glare source at Ivanpah.	51
Figure 39. Parity plot of simulated irradiance vs. measured irradiance at Ivanpah.	51
Figure 40. Ocular hazard plot for glare observed during flyover at Ivanpah between 2014 and 2018. All images yielded a low potential for ocular impact. The yellow dot indicates direct viewing of the sun.	52
Figure 41. Up-aiming strategy can alleviate both glare and avian hazards, but heliostat slew times back to the receiver may be increased.	54
Figure 42. MHT block space (grey) and PV array (blue) in map editor.	60
Figure 43. MHT block space analysis results. Occurrence plot (left) and spatial glare position plot (right) of block space region (light blue).	60
Figure 44. OB vs. OP daily unique glare for MHT.	61
Figure 45. IND map editor display of PV array and encompassing block space (left). Glare analysis occurrence plot (right).	61
Figure 46. OB vs. OP daily unique glare for IND.	62
Figure 47 – Map editor illustrating CPT block space region and PV array to east.	63

Figure 48. CPT block space analysis results. Occurrence plot (left) and spatial glare position plot (right) of block space region (light blue). 63

Figure 49. OB vs. OP daily unique glare for CPT. 64

TABLES

Table 1. List of companies and institutions that received technical assistance during this project. 19

Table 2. Summary of input parameters used in the model. 26

Table 3. Heliostat standby aiming strategies. 29

Table 4. Summary of cumulative hazardous exposure (exceedance) times ($T > 160\text{ }^{\circ}\text{C}$) and normalized annual energy production. 35

1. INTRODUCTION

1.1. Background and Problem Statement

Environmental and permitting requirements have created significant cost and operational impediments to photovoltaic (PV) and concentrating solar power (CSP) development [1-8]. Two issues that have become prominent factors in the siting, permitting, and operation of solar power systems are solar glare, which is relevant to all solar facilities [4, 9], and the potential for birds to be harmed by concentrated solar flux [10-13], which is an issue for CSP power-tower plants.

An example of a solar glare issue is the 530 kW PV installation located near the control tower at Manchester-Boston Regional Airport. The PV system had to be covered with tarp in 2012 after it was found to produce “blinding” glare to air-traffic controllers (Figure 1) [4]. The PV system was eventually reconfigured at a cost of \$2M in 2014 [14]. To address solar glare concerns, the Federal Aviation Administration (FAA) issued a new federal policy in 2013 (78 FR 63276) preventing any new solar energy facilities on federally obligated airports unless a glare study (including ocular impacts) was performed [5]. In 2014, the U.S. Department of Defense (DoD) issued a formal instruction for all military aviation operations to perform glare studies for proposed solar energy systems near their installations [15, 16]. State and local agencies, such as Solano County in California, have also issued recent moratoriums preventing the deployment of solar energy until new policies and methods to mitigate glare can be implemented [17].

An example of the second concern, avian hazards, includes reports of birds being singed by concentrated solar flux at the Ivanpah Solar Electric Generating System (ISEGS), the world’s largest CSP system, located 64 km southwest of Las Vegas, NV [18-23]. These issues have resulted in millions of dollars in additional data collection and reporting costs. Interestingly, the high-flux regions (hot spots) that may be harming birds may be caused by solar reflections from heliostats in standby mode [24], the same cause of intense glare reported by pilots flying over the Ivanpah site (Figure 1). Thus, for CSP plants, the issues of glare and avian mortality may be related and need to be addressed.



Figure 1. Examples of solar glare. Left: PV system at Manchester-Boston Regional Airport viewed from the air-traffic control tower. Right: Glare from Ivanpah CSP plant viewed from an aircraft.

1.2. Objectives

The objectives of this work were as follows:

- Enhance existing tools and develop new methods to better evaluate glare and avian flux hazards from solar energy systems
- Provide training and technical assistance for SGHAT technology and associated tools, and expand the capabilities of the software; license SGHAT to industry
- Develop, test, and validate heliostat aiming strategies that minimize regions of high flux that might be harmful to birds while minimizing negative impacts to plant operational performance

2. SOLAR GLARE HAZARDS AND ANALYSES

2.1. Glare Hazards

Impacts of solar glint and glare on eyesight can include discomfort, disability, veiling effects, after-image and retinal burn [25-28]. Prolonged exposure to “discomfort glare” may lead to headaches and other physiological impacts, whereas “disability glare” immediately reduces visual performance. Disability glare can include after-image effects, flash blindness and veiling, such as that caused by solar glare on a windshield that might mask pedestrians, vehicles, or aircraft. Retinal burn can occur with exposure to lasers or concentrated sunlight.

Ho et al. [29] developed general irradiance models for glare that can be produced by solar reflections and summarized the potential impacts to eyesight as a function of retinal irradiance (the solar flux entering the eye and reaching the retina) and subtended source angle (size of glare source divided by distance). Figure 2 shows the resulting “Ocular Hazard Plot” with three regions: (1) potential for permanent eye damage (retinal burn), (2) potential for temporary after-image, and (3) low potential for temporary after-image. If the retinal irradiance or subtended angle is sufficiently large, permanent eye damage from retinal burn may occur (e.g., from concentrating mirrors). Below the retinal burn threshold, a region exists where a sufficiently high retinal irradiance may cause a temporary after-image, which is caused by bleaching (oversaturation) of the retinal visual pigments. The size and impact of the after-image in the field of view depends on the size of the subtended source angle. For a given retinal irradiance, smaller source angles yield smaller after-images, and the potential impact is less. Sufficiently low retinal irradiances and/or subtended angles of the glare source have a low potential for after-image and ocular impacts.

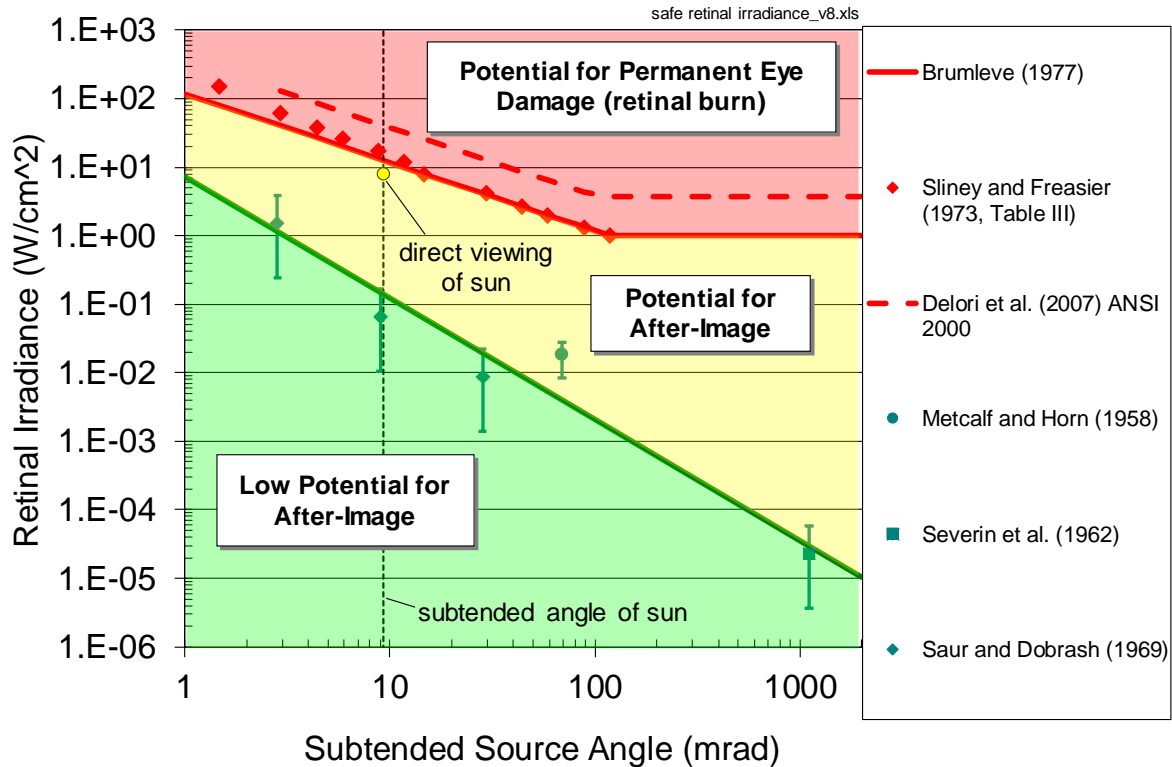


Figure 2. Potential ocular impacts of retinal irradiance as a function of subtended source angle [29]. Note: 1 watt yields approximately 100 lumens of visible light in the solar spectrum.

A number of factors can affect both the intensity and perceived impact of glare: direct normal irradiance (DNI), reflectance, distance, size of the reflecting surfaces, and human factors. The DNI is the amount of solar irradiance striking a surface perpendicular to the sun's rays. A typical clear sunny day may yield a DNI of ~1,000 watts per square meter at solar noon, with lower values in the mornings and evenings. The DNI provides the starting "strength" or irradiance of the solar glare source, and the irradiance can then be reduced by the reflectance of the mirror or receiver. The reflected light can be characterized as a combination of specular (mirror-like) and diffuse (scattered) reflections. Smooth surfaces such as mirrors and smooth glass (on PV modules) produce more specular reflections with greater intensity and tighter beams (larger retinal irradiances and smaller subtended angles used in Figure 2), while solar receivers produce more diffuse reflections with lower solar intensities but greater subtended angles. Typically, specular reflections pose a greater risk for ocular hazards.

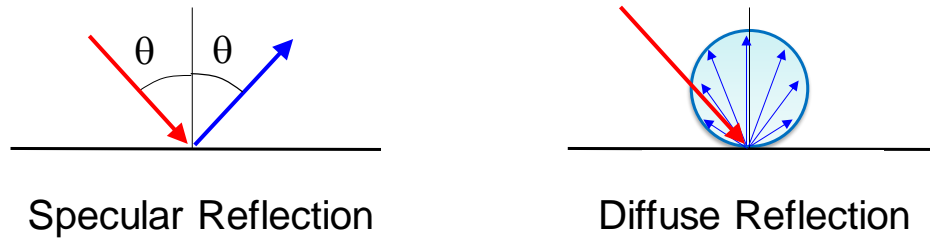


Figure 3. Illustration of specular and diffuse reflections.

The distance between the observer and the glare source can impact both the retinal irradiance and subtended source angle. Atmospheric attenuation caused by particulates or humidity in the air will reduce the retinal irradiance with increasing distance.* In addition, for a fixed size of the glare source, larger distances will typically yield smaller subtended angles of the glare source.

Finally, human factors such as ocular properties (pupil size, eye focal length, ocular transmittance) and light sensitivity will affect the retinal irradiance, subtended angle and perceived impact of the glare. Typical ocular properties for daylight adjusted eyes are provided in Ho et al. [29].

The following section describe tools that can be used to assess glare from solar energy systems.

2.2. Glare Tools

2.2.1. Solar Glare Hazard Analysis Tool (SGHAT)

2.2.1.1. SGHAT Background

Sandia’s patented Solar Glare Hazard Analysis Tool (SGHAT) [30] is an *R&D 100* award-winning software[†] that determines when and where solar glare can occur throughout the year from a user-specified PV array, as viewed from user-prescribed observation points [31]. The potential ocular impact from the observed glare is also determined, along with a prediction of the annual energy production. Configurations can be quickly modified (e.g., tilt, orientation, shape, location) to identify a design that mitigates glare while maximizing energy production. SGHAT technology has been used to assess PV deployments at hundreds of airports in the United States and around the world, at dozens of DoD military installations, and at hundreds of residential and business sites.

SGHAT technology employs a web-based software tool that uses an interactive Google map with drawing and selection tools that allow the user to quickly locate a site, draw an outline of the proposed PV array, and specify observer locations or paths (Figure 4). Latitude, longitude, and elevation are automatically recorded through the Google map interface, providing necessary information for sun position and vector calculations. Additional information regarding the

* Without atmospheric attenuation, the retinal irradiance [W/m^2] is independent of distance since the power entering the eye (numerator) and exposed retinal area (denominator) decrease at the same rate with increasing distance.

[†] SGHAT was freely available as an online tool until 2018. As of July 2018, SGHAT was taken down due to increased cybersecurity restrictions at Sandia. Publicly available licensed versions of SGHAT are listed at www.sandia.gov/glare.

orientation and tilt of the PV panels, reflectance, environment, and ocular factors can be entered by the user. SGHAT can also model fixed-tilt, single-axis, and dual-axis tracking.

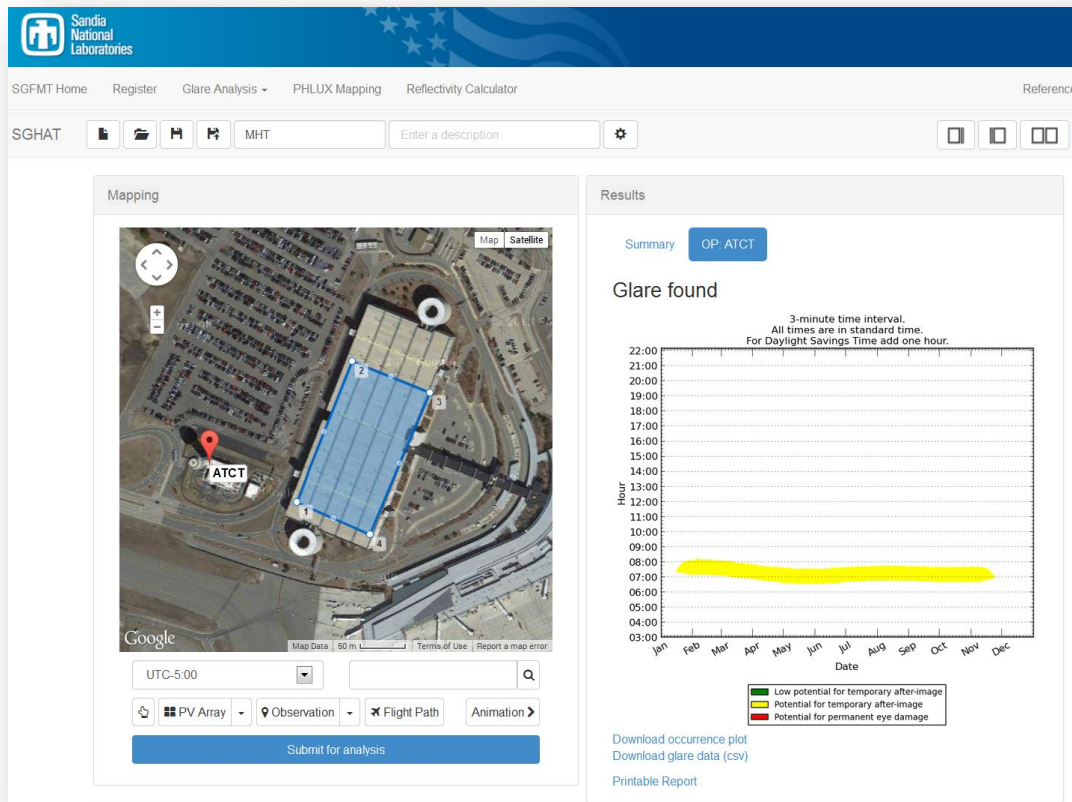


Figure 4. Screen image of SGHAT with Google Map interface and interactive drawing tools to prescribe the location of the PV array (blue outline) and observation points (red marker).

SGHAT calculates the sun position at every minute (or user-specified time-step) throughout the year and determines if glare is visible from the prescribed observation points. If glare is found, the tool calculates the retinal irradiance and subtended angle of the glare source to predict potential ocular hazards.[‡] When the analysis is complete, a summary of the input parameters is shown for the current analysis, along with the annual energy production and Glare Occurrence Plot (Figure 4, right). The Glare Occurrence Plot shows when glare can be observed from the specified observation point(s) at each time step throughout the year. The color of the plotted points indicates the potential ocular hazard. In this example, the yellow dots indicate that the glare has the potential to cause a temporary after-image from approximately February to November for 30 – 40 minutes in the mornings.

[‡] The analysis uses the direct normal irradiance (DNI), which is determined from the user-prescribed peak DNI and irradiance profiles from the National Solar Radiation Data Base (http://rredc.nrel.gov/solar/old_data/nsrdb/).

Finally, SGHAT allows the user to save the data and images to files that can be read by Excel, or output to a report. The FAA has stated that these outputs, which determine when and where glare will occur as well as the potential ocular impacts, will satisfy their interim policy requirements for glare analyses ([78 FR 63276](#)).

2.2.1.2. Enhancements to SGHAT

As part of the current work, enhancements were implemented in SGHAT. These features included new receptor types, integration with the PVWatts API, a 3D visualization of daily glare, and usability improvements.

New Receptor Types. The block space receptor and structure receptor enable users to more accurately model glare impacts on airspace regions and buildings. This feature allows the user to select large regions (rather than individual points) for glare analyses (Figure 5). These receptor types are now available in addition to the existing flight path and discrete point receptors.

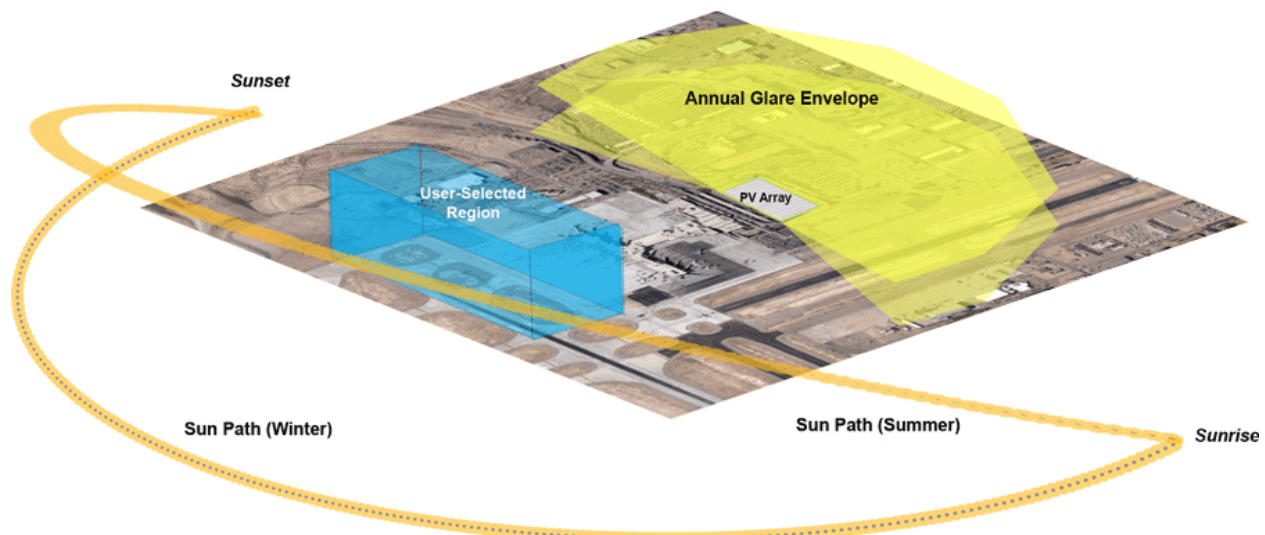


Figure 5. Block space analysis concept. User outlines entire region, such as airport airspace, rather than discrete points.

The new receptor types were validated by comparing their ocular impact results with aggregated results from a set of 250 discrete receptor points placed within the receptor areas (see Appendix A). Three locations were selected for analysis and validation: Manchester Boston Airport (MHT), Indianapolis International Airport (IND), and Cape Town International Airport (CPT). Each site configuration included one photovoltaic array and one outlined region. The CPT site was selected due to its location in the southern hemisphere, to ensure latitude-independent accuracy. In all three trials the correlation coefficient was > 0.99 , indicating successful validation.

PVWatts Integration

SGHAT versions 2 and 3 included a basic calculation for PV system output based on the sun position and DNI. A more accurate determination was added in the form of a PVWatts API query. This new feature accesses the NREL PVWatts API to retrieve estimated system output based on the PV array parameters and system losses.

Initial attempts at validation found that the basic SGHAT calculation over-predicted energy output by differing amounts, depending on the location. A secondary validation was performed in order to understand the discrepancy in over-prediction. Several sites throughout the country were analyzed. This validation found that the varying over-prediction was due to site-specific DNI values used by PVWatts. PVWatts incorporates more accurate location-specific DNI values, whereas the basic SGHAT energy calculation assumes a base DNI of 1000 W/m^2 , which can be set by the user. After adjusting for location-specific DNI variability, the energy prediction from SGHAT matched well with PVWatts when evaluating systems at different times of the year in four cities (Figure 6).

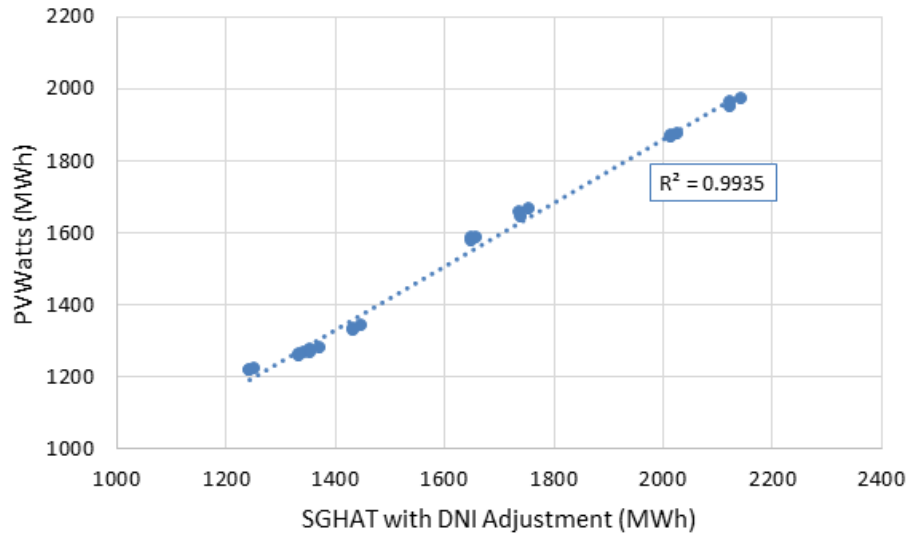


Figure 6. Validation of PVWatts vs. SGHAT, adjusted for weather.

3D Daily Glare Visualization

The Glare Visualization tool provides a graphical interface for displaying glare reflections for each minute of a selected day alongside simulated site components and receptors (Figure 7). Users can navigate the simulation using keyboard shortcuts and can determine glare for receptors by visually inspecting the glare projection for the specified day. The daily glare simulation was validated by comparing its glare predictions with results from a standard glare analysis for five selected days. Visualization results matched expected results in all cases.



Figure 7. Glare Visualization of MHT array (purple) with Air Traffic Control Tower (white), flight path (green), and cumulative daily glare for July 1.

2.2.2. ForgeSolar

Sandia began licensing the SGHAT technology in early 2016 as part of its commercialization plan for the current work. Sims Industries obtained a non-exclusive license to SGHAT in 2016 and launched a commercial version of its analysis tools at www.forgesolar.com. ForgeSolar offers a tiered subscription plan for its tools that provide enhanced capabilities for glare analyses and design optimization. The ForgeSolar deployment has been a commercial success and continues to serve thousands of registered users throughout the world. Information regarding licensing of SGHAT technology is available at www.sandia.gov/glare.



Figure 8. ForgeSolar website (<https://forgesolar.com>).

2.2.3. SolTrace and SolarPILOT

The National Renewable Energy Laboratory's (NREL) SolTrace [32] and SolarPILOT [33] are optical simulation tools specifically designed for CSP systems. SolTrace uses a Monte Carlo ray-tracing algorithm to model radiation from the sun and interactions with a variety of reflecting or absorbing components. Ray-tracing methods can be very rigorous and accurate, but depending on the complexity and size of the modeled domain, the number of rays required can be computationally expensive. The free tool is available for download from NREL (www.nrel.gov/csp/soltrace.html).

SolarPILOT (Solar Power tower Integrated Layout and Optimization Tool) integrates SolTrace within a broader toolset that can generate heliostat field layouts in various patterns, conduct parametric analyses, and optimize system variables (www.nrel.gov/csp/solarpilot.html). In addition, SolarPILOT includes an analytical optical analysis tool based on Sandia's DELSOL3 optical analysis software that implements a fast Hermite polynomial expansion/convolution method.

The current work used these tools to model alternative heliostat aiming strategies at the National Solar Thermal Test Facility (NSTTF) at Sandia and the Ivanpah Solar Electric Generating System to evaluate potential avian-flux hazards (see Section 3.2).

2.2.4. Tower Illuminance Model (TIM)

Sandia has also developed the Tower Illuminance Model (TIM), a software tool that uses interactive 3D graphics to allow users to “fly” over CSP plants and evaluate the flux and ocular hazards at various locations (Figure 9, top). TIM was developed to evaluate solar glare and ocular impacts from concentrating solar power towers [34]. TIM comprises three components: a user-customizable power tower model, an extensible software architecture, and a three-dimensional interactive navigator. Together these components provide a simple interface so the user can easily construct a plant simulation, modify it, and derive useful data on potential glare hazards. Parameters that can be varied include the plant location, date and time, tower dimensions, heliostat dimensions and field layout, heliostat focal length and reflectivity, heliostat aiming strategies, and observer eye properties.

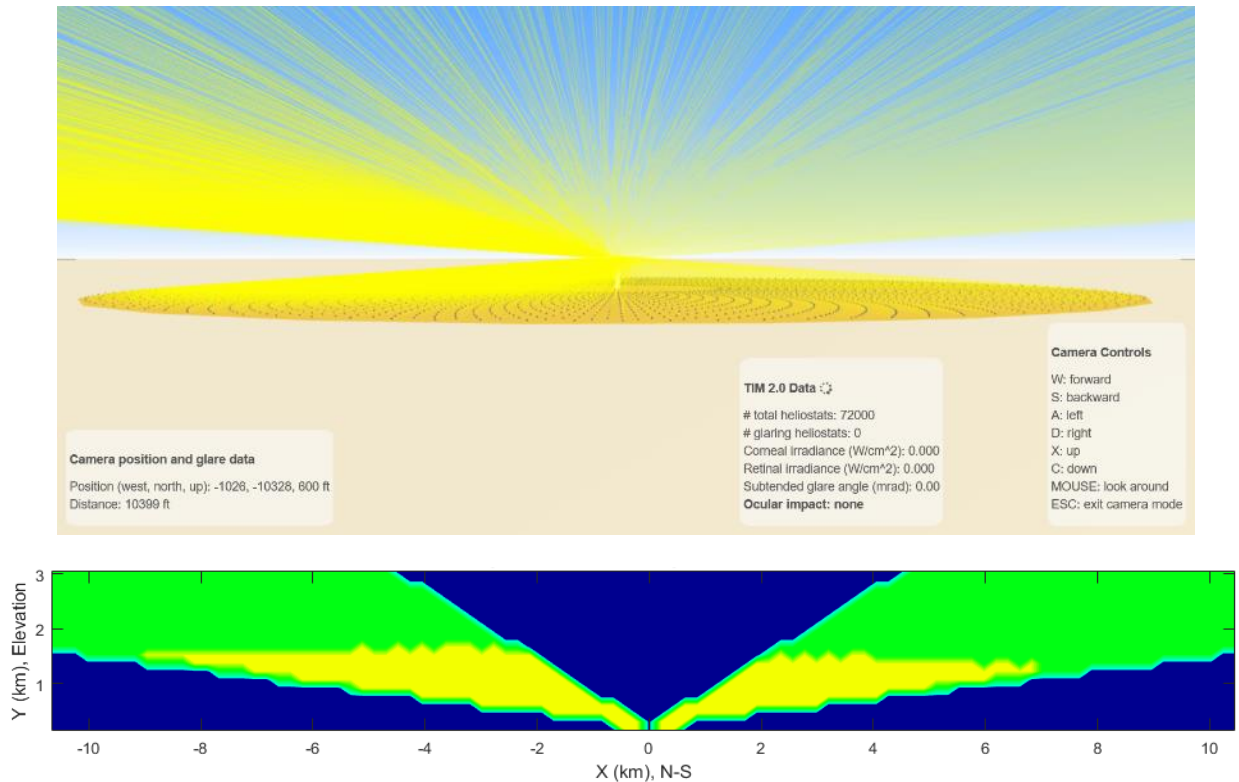


Figure 9. Top: Screen image from TIM software tool. Bottom: Ocular hazard data along a vertical cross-section (green=low potential for ocular impact; yellow= potential for temporary after-image).

For a specified plant configuration, date, and time of day, TIM determines the irradiance, number of heliostats producing glare, and ocular impact at user-prescribed locations in the airspace above the heliostat field (Figure 9, bottom). The ocular impact is determined using the ocular hazard metrics in Figure 2 from the calculated retinal irradiance and subtended source angle. Enhancements to TIM developed as part of the current work include data exporting sampled from grid and transect coordinates, avian glare impact simulation, and aim strategy modeling.

Additional features were also added to TIM that provide many customizable parameters for plant simulation, including:

- Geodetic location and time of day for accurate sun position and tracking
- Power tower location, dimensions, and efficiency
- Field layout (surround vs. polar), dimensions and capacity
- Heliostat specifications including focal length and reflectivity
- Aim strategies including zenithal, annulus, and point-per-group
- Observer eye characteristics

A modular backend architecture was implemented to handle the computational requirements of TIM. The backend utilizes novel glare check algorithms for real-time glare calculations. It determines the irradiance, number of glaring heliostats, and other properties for the user position as they navigate around the field.

The backend architecture includes an extensible component layout for accommodating future tailored plant enhancements. Potential additions include additional field layouts, heliostat aim strategies, and heliostat grouping methods. Standardized code templates provide the building blocks for implementing these enhancements. Existing layouts and aim strategies were implemented using these templates as proofs-of-concept.

2.3. Glare Technical Assistance and Outreach

Our team provided ongoing technical support and assistance to SGHAT users throughout the life of the project. Topics ranged from basic website usage to detailed questions regarding methodology. To date, assistance has been provided to users from over 100 companies and organizations (Table 1). Technical assistance and a detailed glare analysis report was also provided to support the Dubai Electricity and Water Authority (DEWA) IV CSP power tower plant in Dubai, United Arab Emirates [35]. The study investigated the potential glare from the receiver and heliostats, and its potential impact on pilots flying to or from nearby airports.

Sims Industries also provides ongoing assistance to users of its licensed site in the form of email and phone support and free access for non-commercial users, including homeowners and academic entities. The team also presented SGHAT (Version 3) in a webinar hosted by the Solar Energy Industries Association in July 2016. This webinar was attended by various industry and government users.

We also participated in key meetings to address both glare and avian hazards with industry and stakeholders:

- May 24, 2017: Presented summary of glare and avian-flux modeling and impact of alternative aiming strategies at Ivanpah. Participants included NRG, Brightsource, NREL, and Sandia.
- August 16, 2017: Presented summary of work at DOE Technical Symposium on Avian-Solar Interactions in Sacramento, CA. Participants included the Bureau of Land Management, US Fish & Wildlife, USGS, California Energy Commission, ANL, and other stakeholders.

Table 1. List of companies and institutions that received technical assistance during this project.

List of Companies and Institutions that Received Technical Assistance During this Project		
1st Light Energy	Georgia Institute of Technology	Remote Imagery Technologies Inc
Adelante Energy, Inc.	Haley & Aldritch, Inc.	Republic of Korea Air Force
AECOM	Haley Aldritch	Sadler Solar
AFCEC	Heliene Solar	Safari Energy
Alder Energy	HMMH	Saratoga Associates
Alton Group	HOA	Skytech Solar
Anbaric Microgrid LLC	Humboldt State University	Socore Energy
Apricity Renewables, Inc.	Innovative Solar	Sol Energy
ARM Group, Inc.	Innovision Media Ltd.	Solar Omaha
Arup	Ion Solar	SolarCity

List of Companies and Institutions that Received Technical Assistance During this Project		
Associated Engineering	Jade Mountain	Solas Energy Consulting
Aurecon	JDA Solutions	SOLAS Energy Consulting
Azimuth Energy	JDS Power	Solkompaniet
BBP	Johnson Controls	SolPEG GmbH
Belmont Goes Solar	kas green energy	SolUnesco
Blue Oak Energy	Kleinfelder	South Mountain Company
C&S Companies	Landrum & Brown	Southern Current LLC
CA Sun Systems	Lean Corp.	Spacial Solutions
Caldwell County, North Carolina	Lean Engineering	Spohnheimer Consulting
Canadian Solar, Inc.	LSA	Stanley Group
CanadianSolar	Luma Lighting Design	Stantec
Capitol Airspace Group	Luminate, LLC	Studio Santi
Centroplan USA, LLC	Mahindra	Sullivan Solar Power
City of Tallahassee	Mangan	Sumter County, South Carolina
CNC Project Management Pty Ltd	MC Power	Sunlight and Power
Coronal Energy	Millenium 3 Energy	Sunlight Solar
Cranfield University (UK)	MnDOT Office of Aeronautics	Sunpower
CSIRO	Mott MacDonald Construction	SunRun
Cypress Creek Renewables	Navatek, Ltd.	Sunsense, Inc.
DAR	Netsun Energy	SWCA Environmental Consultants
DAR group	Noresco	Swindon, Springer & Co.
DP Energy	NOVA Consultants, Inc.	TESLA
East Midlands Airport	NREL	The etica group
Eien Engineering	Oakleaf Partners	Tritium3
Eisenbach and Ruhnke Engineering, P.C.	Oneida Nation	U.S. Air Force
Elemental Energy	Origis Energy	U.S. Air National Guard
Energy Aware	Orion Power	U.S. DoD
EnterSolar	Osprey Consulting	U.S. DoD Siting Clearinghouse
Enviro Consultants	OST Energy	U.S. FAA
Environmental Ethos	Pager Power	University College Dublin
Environmental Management Associates, Inc.	Perimeter Solar	University of Wisconsin
Envirovision	POWER Engineers, Inc.	Urban Grid
Epuron	Power Water Corporation	Various homeowners and homeowner's associations
EVS, Inc.	Pure Power Engineering	Wardell Armstrong, LLP
FARO Energy	Radiant Energy & Power, Inc.	WEST Environmental and Statistical Consultants
Galetech Energy Services	Rand Enterprises	Westwood
Gen Mounts	Ranger Solar	Wikiwiki Electric, LLC
Geolyse Pty Ltd	Red P LLC	WSP USA

A certification-level training course was developed for users interested in mastering the concepts behind SGHAT. This training teaches the science of glare, the impact of analysis parameters, and potential mitigation strategies. The course is offered via webinar over several sessions, emphasizing hands-on iterative learning for attendees. Additionally, users complete multiple Case Studies and a final Certification Exam. Sims Industries has already conducted successful training courses and currently has a waitlist of interested registrants.

Figure 10 plots the number of new registrations for SGHAT and ForgeSolar tools by quarter since 2013. In 2016, when the ForgeSolar tools became available to the public, registration began shifting from SGHAT to ForgeSolar. The current work included a commercialization plan to license SGHAT to industry so that it could be maintained and serviced beyond the project’s current funding. The successful licensing of SGHAT to ForgeSolar accomplished one of the major objectives and milestones of this work. Figure 11 shows the total PV capacity analyzed using SGHAT technology since 2013 based on projects submitted for analyses (note that not all projects analyzed were constructed).

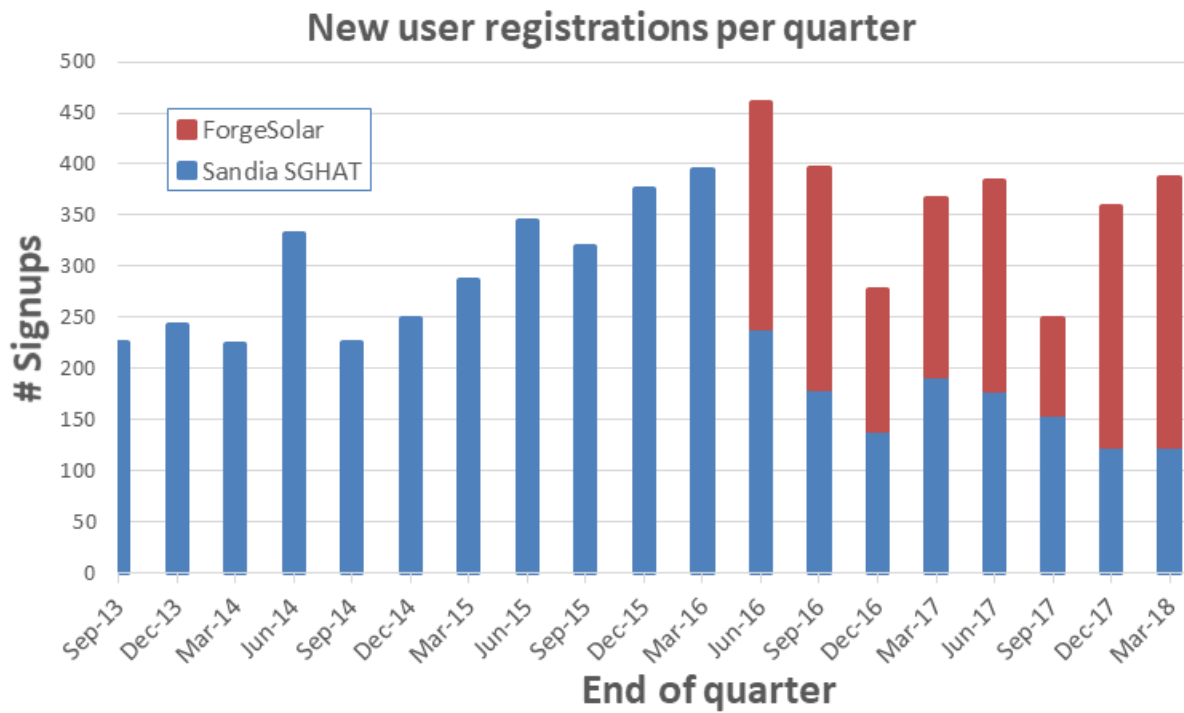


Figure 10. Number of registrations for SGHAT or ForgeSolar tools by quarter.

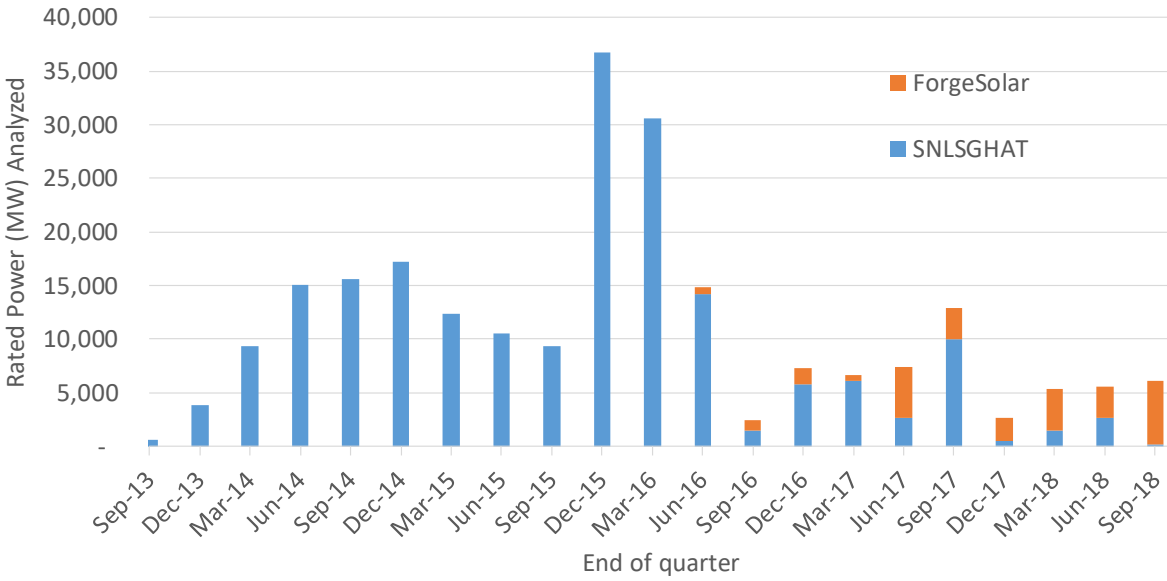


Figure 11. Total PV rated capacity (MW) analyzed using SGHAT technology.

2.4. Summary

Glare hazards may exist at solar energy installations, including PV arrays and heliostats and receivers at CSP plants. Tools such as SGHAT and ForgeSolar can be used to evaluate potential glare from PV arrays and alternative designs that can mitigate glare while maximizing energy production. The current work has developed several enhancements to SGHAT, including block-space receptor models, integration of PVWatts, and a 3D daily glare visualization feature. SGHAT technology has been licensed to Sims Industries, which released the ForgeSolar suite of glare analysis tools and has been a commercial success. Ray-tracing tools such as SolTrace provide more rigorous optical analyses for both PV and CSP systems, but they are computationally more expensive. Regarding analysis of glare from CSP power towers, a fast interactive tool called TIM (Tower Illuminance Model) has been developed as part of the current work that allows glare analyses from various heliostat field configurations. The user can “fly” through the airspace to determine the irradiance and potential ocular hazards at any location.

3. SOLAR FLUX HAZARDS AND ANALYSES

3.1. Introduction to Avian Flux Hazards

Reports of birds being singed by concentrated sunlight from heliostat fields at concentrating solar power plants were first reported by McCrary et al. in the 1980’s at the Solar One power tower pilot plant [12, 24]. They concluded that the primary hazard was from heliostats in standby mode that reflected and concentrated the sunlight toward locations around the receiver (rather than on the receiver). Because the air around the receiver is optically transparent to the irradiance, the birds cannot feel thermally emitted heat from high-flux regions around the receiver, as opposed to the high-temperature receiver itself that emits a considerable amount of thermal radiation.

More recently, reports of avian mortality caused by singeing in high-flux regions in the air space above the heliostat fields at the Ivanpah Solar Electric Generating System in southern California (near Las Vegas, Nevada) have been documented (Figure 12) [11, 19-21, 23, 36, 37]. The operators of Ivanpah have been actively engaged in methods to reduce avian mortality through the use of bird deterrents and alternative heliostat standby aiming strategies. Recent attempts to spread the standby aim points have apparently reduced the irradiance levels. In addition, reports submitted to the California Energy Commission have concluded that Ivanpah has had “low” levels of impacts to local, regional, and national bird populations at a species level (<https://efiling.energy.ca.gov/Lists/DocketLog.aspx?docketnumber=07-AFC-05C>).

The purpose of this work is to develop a model to assess the impact of alternative heliostat standby aiming strategies and resulting irradiance distributions on avian exposure hazards. In addition, a model is developed to assess the impact of additional heliostat slew times resulting from the different aiming strategies on the annual energy production of the plant. Results are presented for nine different heliostat standby aiming strategies using the Ivanpah Unit 2 power tower as a case study, and recommendations for future studies and improvements are discussed.



Figure 12. Left: Illuminated standby aim points next to the receiver at Ivanpah using original aim-point strategy before changes were made. Right: MacGillivray Warbler with “Grade 3” solar flux injury found at Ivanpah [19].

3.2. Modeling Approaches to Evaluate Avian Flux Hazards

3.2.1. Energy Balance and Bird Feather Heating

Previous researchers have tried to identify safe irradiance (flux) levels that would serve as a threshold to mitigate avian hazards. The impact of radiative exposures to birds is expected to depend on both the magnitude of the flux and the exposure time. For example, Santolo [38] described experiments in which they irradiated bird carcasses at different flux levels and durations. They concluded that “no observable effects on feathers or tissue were found in test birds where solar flux was below 50 kW/m^2 with exposure times of up to 30 seconds.” Tyler et al. [39] developed mathematical models of bird-feather heating and found that “a threshold of safe exposure does not exist above a solar flux density of 4 kW/m^2 for a one-minute exposure.” Tyler et al. found 60-second exposures to solar flux greater than 4 kW/m^2 resulted in bird-feather

temperatures above 160 °C, which can compromise the keratin molecular structure and permanently weaken the feathers [39, 40].

In this work, we use a transient mathematical model to determine the bird-feather temperature as a function of irradiance, which is a function of the flight path and heliostat aiming strategy, and other parameters. The transient model is based on an energy balance of the feather (Figure 13) that considers solar irradiance, thermal emittance, and convection [39, 41].

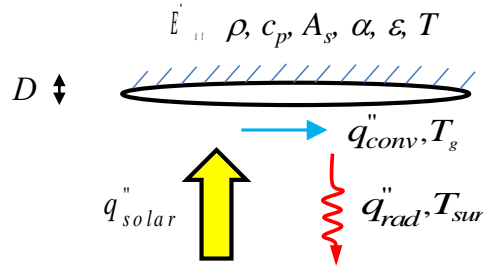


Figure 13. Energy balance on control volume of feather barb exposed to solar irradiance.

Details of the model were introduced in [41] and are summarized here for completeness. Neglecting temperature gradients in the feather [41], an energy balance on the feather yields the following expressions:

$$\dot{E}_{st} = \dot{E}_{in} - \dot{E}_{out} \quad (1)$$

$$(\rho c_p)(A_s D) \frac{dT}{dt} = \alpha q_{solar}'' A_s - q_{conv}'' A_s - q_{rad}'' A_s \quad (2)$$

or

$$\rho c_p D \frac{dT}{dt} = \alpha q_{solar}'' - h(T - T_g) - \varepsilon \sigma (T^4 - T_{sur}^4) \quad (3)$$

where

- \dot{E}_{st} = Rate of energy stored in feather (W)
- \dot{E}_{in} = Rate of energy entering feather (W)
- \dot{E}_{out} = Rate of energy leaving feather (W)
- q_{solar}'' = Solar irradiance (W/m²)
- q_{conv}'' = Convective heat flux (W/m²)
- q_{rad}'' = Thermal emissive flux (W/m²)
- A_s = Surface area of feather exposed to irradiance (m²)
- ρ = Feather density (kg/m³)
- c_p = Feather specific heat (J/kg-K)
- D = Thickness of feather (m)
- h = Convective heat transfer coefficient (W/m²-K)
- t = Time (s)

- T = Temperature (K)
 T_g = Ambient gas temperature for convective heat loss (K)
 T_{sur} = Surrounding temperature for radiative heat loss (K)
 V = Feather volume (m^3) = $A \times D$
 α = Solar absorptance of feather (-)
 ε = Thermal emittance of feather (-)
 σ = Stefan-Boltzmann constant ($5.67e-8 \text{ W/m}^2\text{-K}^4$)

Integrating Eq. (3) yields the following expression:

$$\int_{T_i}^{T_{i+1}} \rho D c_p dT = \int_{t_i}^{t_{i+1}} \left(\alpha q_{solar}'' - h(T_i - T_g) - \varepsilon \sigma (T_i^4 - T_{sur}^4) \right) dt \quad (4)$$

or

$$T_{i+1} = T_i + \frac{1}{\rho D c_p} \left(\alpha q_{solar}'' - h(T_i - T_g) - \varepsilon \sigma (T_i^4 - T_{sur}^4) \right) \Delta t \quad (5)$$

Where i is the time step and Eq. (5) is solved by marching forward in time where $\Delta t = t_{i+1} - t_i$. The thermal properties of air (kinematic viscosity, thermal conductivity, Prandtl number) are a function of the film temperature (average of air temperature and feather temperature) and change as the feather temperature changes. Polynomial functions for these thermal properties were derived from data from [42]. The heat transfer coefficient, h , was determined from the Nusselt number, which was calculated based on the Blasius solution for steady, incompressible, laminar air flow over the feather:

$$Nu = \frac{hL}{k_{air}} = 0.664 Re_L^{1/2} Pr^{1/3} \quad (6)$$

where

$$Re_L = \frac{uL}{\nu} \quad (7)$$

and L is the characteristic length (m) of the feather parallel to air flow, k_{air} is the thermal conductivity of air (W/m-K), Pr is the Prandtl number (ratio of momentum and thermal diffusion), u is the air velocity over the feather (m/s), and ν is the kinematic viscosity of air (m^2/s). Table 2 shows the parameter values that are used in this study and associated references. The solar absorptance and thermal emittance of the feather are assumed to be equal, and they account for the radiative view factor for solar irradiance on the feather and thermal emission to the environment.

Table 2. Summary of input parameters used in the model.

Parameter	Value	Reference / Comments
Thickness of feather* (m), D	1.00E-04	Based on thickness of barbule [39, 43, 44]
Characteristic length of feather (m), L	0.15	From [39]
Heat capacity of feather ($\rho \cdot c_p$) (J/m ³ -K)	2.0E+06	From [39]
Air velocity over feather (m/s), u	8	Assumed
Thermal conductivity of feather (W/m-K), k_{air}	0.04	Used to determine heat transfer coefficient from calculated Nusselt number [45, 46]
Heat transfer coefficient (W/m ²), h	28	Calculated from air velocity and thermal properties
Surround temperature for convection and radiation (K), T_{sur}	298	From [39]
Effective feather absorptance or emittance, α or ϵ	1	Assumed for black feather
Initial feather temperature (K)	298	Assumed
Irradiance (W/m ²), Q	Variable	Depends on location and heliostat aiming strategy

*The diameter of individual barbules has been reported to be ~2 – 6 microns for goose feathers, and the thickness of the ramus holding the barbules has been reported to be ~70 microns in ospreys [44]. For the purposes of this heat-transfer analysis, we assume the baseline thickness of the barb to be ~100 microns.

Probabilistic results from [41] showed that the most important parameters impacting the modeled temperature rise were the irradiance (positive correlation), feather thickness (negative correlation), absorptance (positive correlation), and feather heat capacity (negative correlation). The irradiance depends on the bird flight path and heliostat aiming strategy (Figure 14), which were varied. The other parameters were kept constant. The bird flight paths were assumed to be straight lines spaced 20 m apart along horizontal transects (sensitivity studies varying the spacing from 1 m – 100 m did not show a change in the results). The cases considered are summarized as follows:

- Straight flight paths spaced 20 m apart along the east-west and north-south directions along horizontal transects
- Seven horizontal transects at elevations of 80, 100, 122 (receiver midplane), 140, 160, 180, and 200 m
- Nine heliostat standby aiming strategies (see next section)
- Two times of the day (solar noon and 3 hours before solar noon)
- Four days of the year (winter solstice, spring equinox, summer solstice, fall equinox)

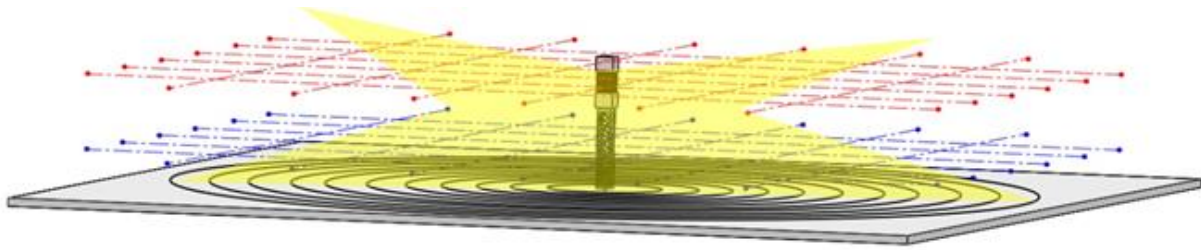


Figure 14. Illustration of the illuminated air space above the heliostat field at Ivanpah and bird flight paths.

Figure 15 shows an example of flight paths superimposed on an aerial view of a simulated flux map along a horizontal plane in the air space above Unit 2 at Ivanpah that were used to calculate the bird feather temperatures. In this study, we focus on identifying alternative heliostat standby aiming strategies that minimize the time that bird-feather temperatures exceed 160 °C.

SolTrace is used to rigorously characterize the irradiance profiles for different heliostat standby aiming strategies and to determine associated bird feather temperatures (see Section 3.2.2). A path simulation tool was also implemented in TIM to model the incoming irradiance on a bird, as well as its feather temperature, as it travels between two points near the CSP field. The TIM avian path functionality allows a user to select two points, signifying the start and end points of an avian flight path. TIM simulates the heliostat field and flux impacts on the bird while it travels along the designated flight path. Using Eq. (5) and an analytical irradiance model [29], TIM determines the feather temperature and incoming flux on the bird throughout its flight and generates relevant plots. These can be used to pinpoint when a safe temperature threshold is exceeded.

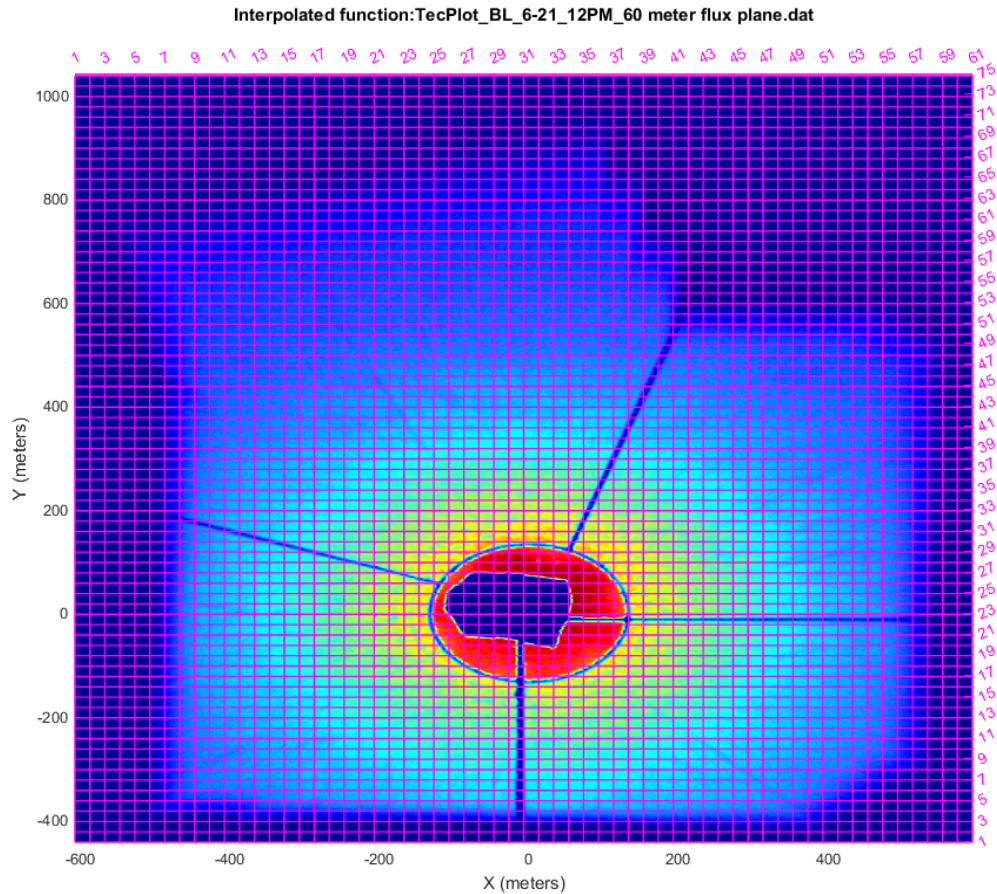


Figure 15. Sample of flight paths superimposed on plan view of simulated flux map over Ivanpah Unit 2.

3.2.2. Evaluation of Alternative Heliostat Standby Aiming Strategies

Because each heliostat aiming strategy yields uniquely different flux profiles in the airspace above the heliostat field, multiple horizontal transects at regularly spaced elevations were used to define bird flight paths at different times of the day and different days of the year. The bird-feather temperature along each flight path was calculated, and the cumulative amount of time exceeding 160 °C was recorded for each heliostat standby aiming strategy.

In addition to a baseline heliostat standby aiming strategy, eight alternative aiming strategies were evaluated (Table 3). The baseline aiming strategy assumed all standby heliostats were aimed in a clockwise direction along a 25-m radial ring around the midplane of the receiver. Options 1 – 6 spread the aim points azimuthally by increasing the radial distance of the aim points around the receiver from 25 – 250 m. The aim point within this region was randomly selected for each heliostat. Option 1 retained the clockwise aiming direction around the receiver, but Options 2 – 6 introduced random aiming directions in both the clockwise and counterclockwise directions (results showed that clockwise vs. counterclockwise aiming directions did not significantly impact the results). Options 2 and 6 were implemented at Ivanpah, and monitoring studies are ongoing to evaluate impacts on avian mortality.

In addition to the six alternative aiming strategies that spread the aim points around the receiver, two additional point-focus heliostat standby aiming strategies were also evaluated. In these two cases, all of the standby heliostats were aimed at a prescribed location above the receiver. It was postulated that although the flux at the single aim points would be extremely high, the total volume of hazardous flux would be reduced.

Table 3. Heliostat standby aiming strategies.

Aiming Strategy	Description
Baseline	Standby heliostats aimed along a 25 m radial ring around the receiver in a clockwise direction
Option 1	Standby heliostats aimed along a 25 – 60 m radial ring around the receiver in a clockwise direction
Option 2	Standby heliostats aimed along a 25 – 60 m radial ring around the receiver in both clockwise and counterclockwise directions
Option 3	Standby heliostats aimed along a 25 – 100 m radial ring around the receiver in both clockwise and counterclockwise directions
Option 4	Standby heliostats aimed along a 25 – 150 m radial ring around the receiver in both clockwise and counterclockwise directions
Option 5	Standby heliostats aimed along a 25 – 200 m radial ring around the receiver in both clockwise and counterclockwise directions
Option 6	Standby heliostats aimed along a 25 – 250 m radial ring around the receiver in both clockwise and counterclockwise directions
Point Focus 160m	Standby heliostats aimed at a single point 20 m above the top of the receiver (160 m above ground level)
Point Focus 180m	Standby heliostats aimed at a single point 40 m above the top of the receiver (180 m above ground level)

Figure 16 shows the geometry and dimensions that were used to calculate a safe distance above the receiver to avoid excessive irradiance on the top of the receiver shield. Based on the closest heliostats, the minimum distance above the receiver was calculated to be 20 m, or 160 m above the ground. Two point-focus scenarios with aim points at 160 m and 180 m above the ground were evaluated.

The SolTrace optical modeling tool was used to generate flux maps over the Ivanpah Unit 2 heliostat field. In cooperation with NRG, operator of the Ivanpah plant, data and information on the heliostat design and field configuration were obtained and imported to SolTrace. High resolution maps of the flux (kW/m^2) were generated for seven horizontal transects, two times of the day, four days of the year, and nine heliostat standby aiming strategies for a total of 504 flux maps that provided the irradiance distribution for the bird-feather temperature modeling described in Section 3.2.1. All heliostats in Unit 2 were assumed to be placed in the selected standby mode for each aiming strategy.

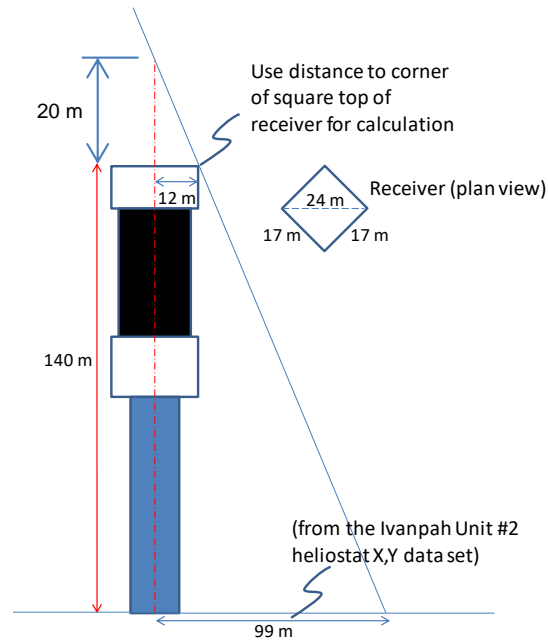


Figure 16. Dimensions used to calculate safe distance above receiver for a single point-focus aim point directly above the receiver.

3.2.3. Heliostat Slew Times and Annual Performance

For each alternative heliostat standby aiming strategy, the cumulative time required for the heliostats to move from the standby aim point to the receiver target (slew time) is determined based on an assumed rotational speed of the azimuthal and elevation drives.[§] The ratio of the slew time for alternative standby aiming strategies to that of the baseline aiming strategy is used to define a slew-time ratio (multiplier). The product of the slew-time ratio and the start-up time for the baseline case (prescribed to be 30 minutes) is then used to estimate the impact of additional slew time, if any, on energy production via an increase in a proxy start-up time. The absolute values of annual energy production should not be construed as accurate; rather, the trends of impact of alternative standby aiming strategies on the annual energy production can be used to identify which strategies show promise. For example, if the slew times between an alternative strategy and the baseline are the same, then the impact on annual energy production can be assumed to be negligible.

The System Advisor Model [47] was used to evaluate the impact of alternative standby aiming strategies and slew times on annual energy production of Unit 2 at Ivanpah. Figure 17 shows the impact of start-up times on the simulated annual energy production. The simulated annual energy production remains constant until the start-up time reaches ~70 minutes. As start-up times increase beyond ~70 minutes, the simulated annual energy production decreases. For example, if the slew-time ratio for an alternative aiming strategy was determined to be 5 relative to the baseline (due to

[§] The rotational speed of the heliostat drives is assumed to be ~24 degrees/minute based on the heliostats at the National Solar Thermal Test Facility at Sandia. With this speed, the slew time is calculated using the heliostat and receiver coordinates and prescribed aim points. Although the drive rates of the heliostats at Ivanpah are likely to be different, assuming a constant value allows comparison among different aiming strategies.

increased spreading of the aim points), Figure 17 shows that the calculated proxy start-up time of 5 x 30 minutes = 150 minutes would yield an annual energy production that is ~85% of the baseline annual energy production. The use of a proxy start-up time is a simplified approximation, but it provides a measure of the impact of the heliostat slew times on annual energy performance. The overall objective is to minimize the bird-feather temperatures while maximizing the annual energy production.

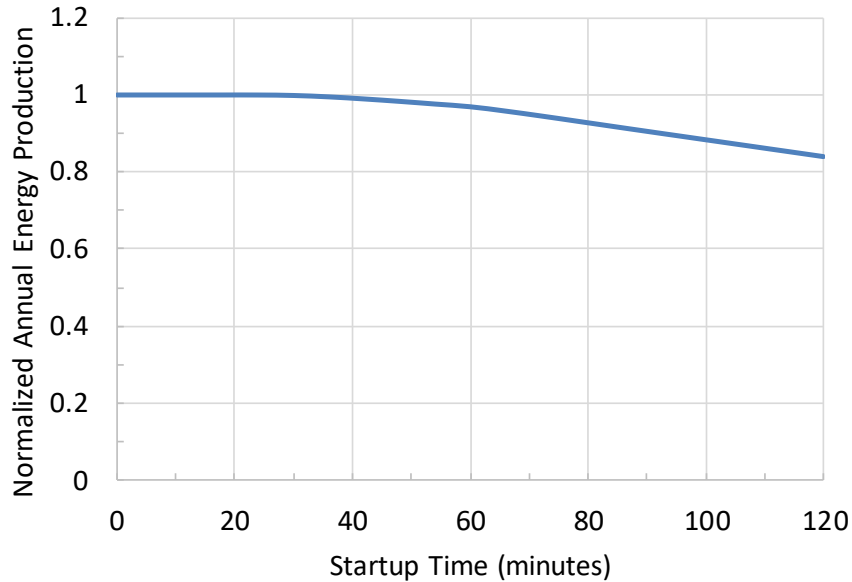


Figure 17. Impact of startup time on annual energy production normalized to 30-minute startup time.

3.3. Results

3.3.1. Flux Maps

Figure 18 shows sample results of simulated flux maps for three alternative heliostat standby aiming strategies along horizontal transects at three different elevations. The baseline flux maps show a higher concentration at the midplane of the receiver relative to the other options that spread the aim points. Recall that in the baseline case, all of the standby heliostats were aimed along a ring with a radius of 25 m around the center of the receiver. Option 3 spread the aim points around a 25 – 100 m annulus around the receiver, and Option 6 spread the aim points around a 25 – 250 m annulus around the receiver. Those options show a lower flux along each of the three transects shown in Figure 18.

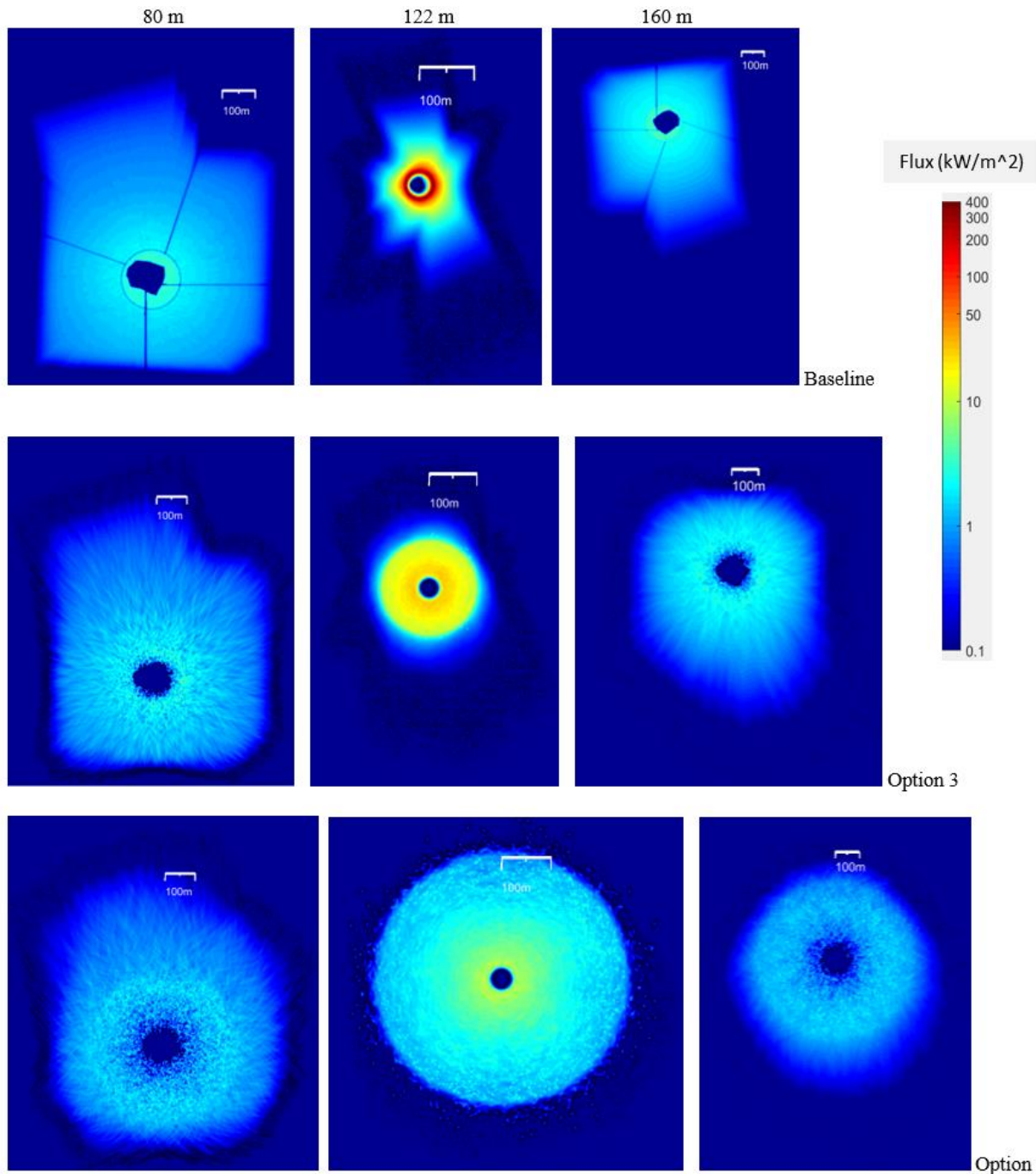


Figure 18. Flux maps at three different elevations (80, 122 (receiver midplane), and 160 m) for three heliostat standby aiming strategies (Baseline, Option 3, and Option 6) at solar noon on the summer solstice.

Figure 19 shows several flux maps for the point-focus scenario with all standby heliostats aimed at a single point 20 m above the top of the receiver. The flux maps indicate that large regions of high-flux conditions exist, despite the original hypothesis that a single aim point might limit the extent and duration of hazardous exposure to birds. The results in the next section confirm that a

single point-focus standby aiming strategy actually increases the hazardous exposures due to the high flux levels extending around the focal point.

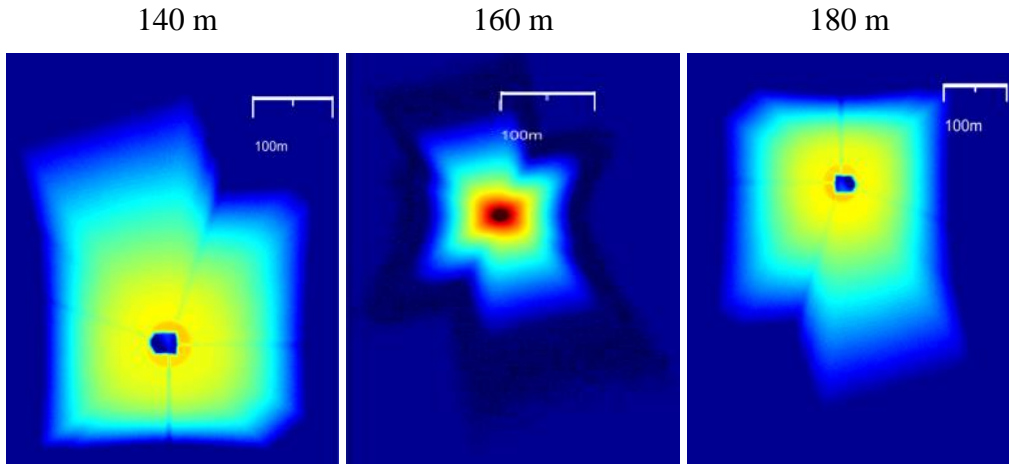


Figure 19. Flux maps at different elevations with all standby heliostats aimed at a single point 20 m above the top of the receiver (160 m elevation) at solar noon, summer solstice.

3.3.2. Avian Flux Hazard and Impact on Annual Operating Performance

Together with the irradiance values from the 504 flux maps described in the previous section, Eq. (5) and the parameter values in Table 2 were used to determine the bird-feather temperature along the various flight paths, transects, dates, and times described in Section 3.2.1.

Figure 20 shows an example of the modeled bird-feather temperatures for a single flight path analyzed at the 122-m elevation transect at solar noon on the summer solstice. As the bird travels through the high flux region (from north to south), its feather temperature increases due to the increasing irradiance. The “hole” in the middle of the high-flux region causes the feather temperatures to decrease temporarily as the convective and radiative heat losses allow for cooling. The feather temperatures increase again as the bird flies through the other side of the high-flux annulus region. As the bird flies out of the high-flux region, the feather temperatures decrease to initial conditions. The cumulative amount of time that the feather temperature exceeded 160 °C was recorded for each flight path, elevation transect, date, time, and heliostat standby aiming strategy simulated, and the results are summarized in Table 4.

Table 4 summarizes the total time that the bird-feather temperature exceeded 160 °C for each of the heliostat standby aiming strategies. Results show that relative to the baseline strategy with a fixed-radius aim point of 25 m, spreading the aim points up to ~100 m increased the exceedance time by up to 14 %. Spreading the outer annulus of the aim points to 150 m (Option 4) or larger showed a decrease in exceedance times. With a spread in the aim points out to 250 m (Option 6), the cumulative bird-feather temperature exceedance time decreased to 10% of the baseline. However, as the outer radius of the aim-point annulus increased to 150 m (Option 4) and higher, the simulated annual energy production decreased due to the increased slew times and impact on proxy start-up times. Option 6 showed that the simulated annual energy production was reduced by 23%.

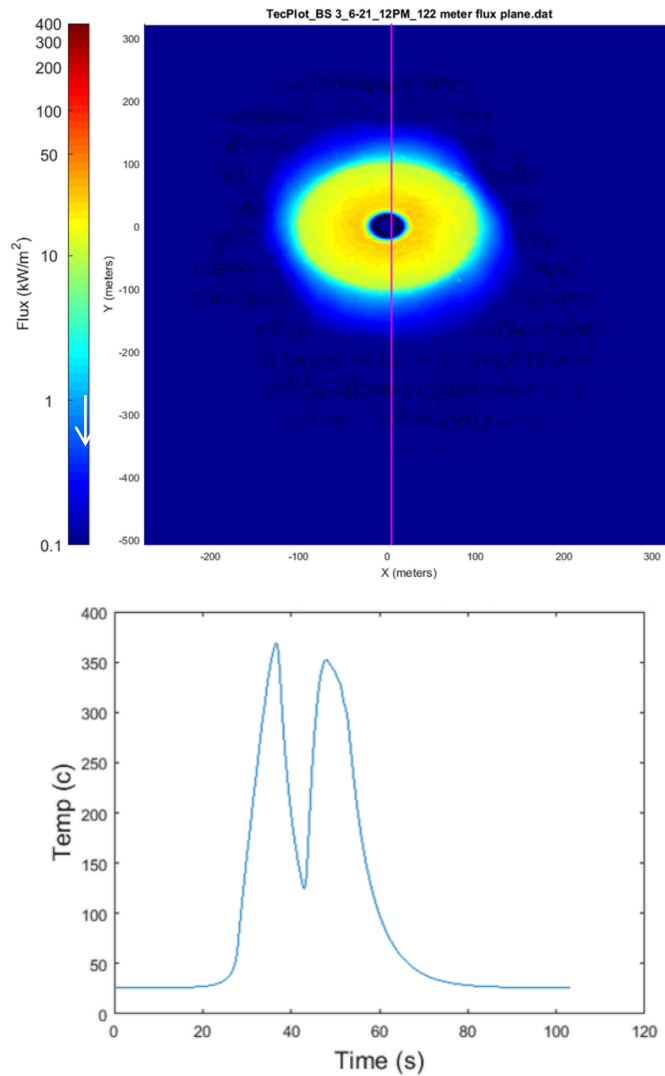


Figure 20. Example of modeled bird-feather temperatures along a single flight path (flying from north to south) along a horizontal transect (Option 3, 122 m elevation).

Interestingly, the two point-focus strategies that aimed all of the standby heliostats at a single point above the receiver yielded greater hazardous exposures (bird-feather temperatures exceeding 160 °C) relative to the baseline (38% - 45% higher). Although all of the standby heliostat were aimed at a single point, the beams overlapped in regions extending all around the focal point, creating large regions of high irradiance that yielded hazardous bird-feather temperatures.

Table 4. Summary of cumulative hazardous exposure (exceedance) times ($T > 160\text{ }^{\circ}\text{C}$) and normalized annual energy production.

Heliostat Aiming Strategy	Exceedance Time (s) ($T > 160\text{ }^{\circ}\text{C}$)	Exceedance Time Normalized to Baseline	Annual Energy Normalized to Baseline
Option 1 (25-60 m CW)	4752	1.05	0.98
Option 2* (25-60 m)	4799	1.06	0.98
Option 3* (25-100 m)	4986	1.1	0.95
Option 4* (25-150 m)	3501	0.77	0.9
Option 5* (25-200 m)	1466	0.32	0.85
Option 6* (25-250 m)	560	0.12	0.81
Point Focus (160 m)	6291	1.39	1
Point Focus (180 m)	6192	1.37	1

CW = clockwise aiming direction around receiver

*Standby heliostats aimed in both directions around receiver

Figure 21 shows a plot of the normalized hazardous exposure times exceeding $160\text{ }^{\circ}\text{C}$ and the normalized annual energy production relative to the baseline values. As the hazardous exposure times are reduced, the annual energy production is also reduced due to increased heliostat slew times and proxy start-up times. Thus, current results suggest that Options 4 and 5 may yield the best combination of reducing avian flux hazards while minimizing impacts on operating performance, but conclusions depend on the relative value placed on plant performance vs. avian safety. Additional strategies could also be implemented to further reduce negative impacts on operational performance, such as sequential rather than simultaneous movement of heliostats from standby position to the receiver. Thus, alternative standby aiming strategies that significantly reduce avian flux hazards could be considered without negatively impacting operational performance.

Another consideration in the effort to optimize heliostat aiming strategies is the potential for glare from the heliostats in standby mode. Ivanpah is situated near several airports, including McCarran International Airport in Las Vegas, NV. Pilots have reported issues of glare from the heliostats at Ivanpah, and studies have shown that the glare is a result of heliostats in standby mode [29, 48, 49]. Therefore, simply spreading heliostat aim points to reduce avian flux hazards will likely not alleviate glare (and may even exacerbate the problem by creating a larger volume of airspace subject to glare). Alternative mitigations that consider directional and time-of-day aiming strategies for air traffic, dynamic heliostat aiming strategies, bird deterrents, and flux/glare shields need to be evaluated to further reduce hazards associated with both solar flux and glare. One strategy, “up-aiming,” that has recently been investigated reflects the light vertically upward (or within $30 - 40$ degrees of zenith) during standby conditions and yields no additional exceedance times or predicted avian flux hazards while also mitigating the impacts of glare. Although the individual heliostat slew times were increased, this strategy may be very beneficial if sequential movement strategies can be implemented to minimize the impact on operational performance.

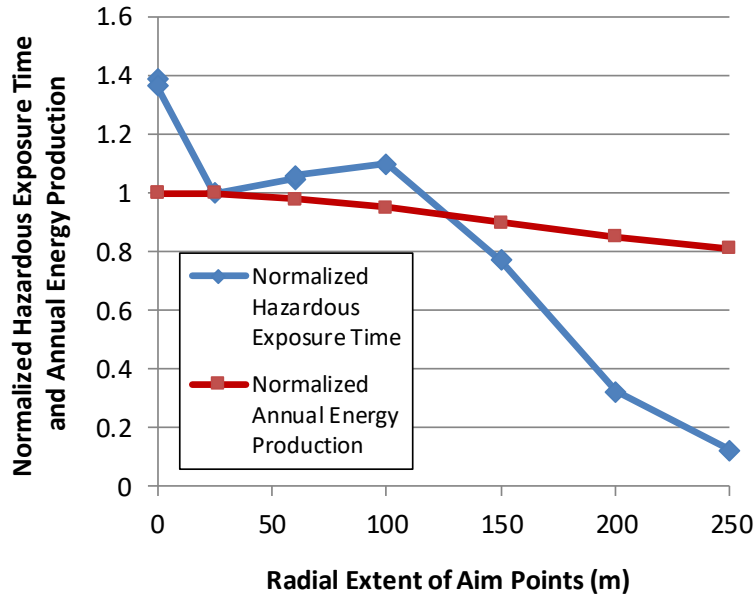


Figure 21. Plot of normalized performance metrics as a function of radial extent of aim points.

3.3.3. Summary

High-flux regions in the airspace above heliostat fields can cause exposure hazards to birds and other avian species. Previous work has indicated that the primary hazards are caused when heliostats are in standby mode and aimed at locations around (rather than on) the receiver.

The current work presents a study of alternative heliostat standby aiming strategies and their impact on avian exposure hazards. A model was developed to assess the bird-feather temperature as a function of solar irradiance, thermal emittance, and convection as the bird flies through the airspace above the heliostat field. A total of 504 flux maps covering seven elevation transects, two times of the day, four days of the year, and nine aiming strategies were developed using a ray-tracing model of the Ivanpah Unit 2 heliostat field. Results showed that spreading the radial aim points out to ~150 m and greater reduced the cumulative time that feather temperatures exceeded the hazard metric of 160 °C (the temperature at which feathers can be permanently weakened). Results also showed that aiming all of the standby heliostats at a single point above the receiver increased the hazardous exposure times due to the large amount of overlapping beams around the focal point.

The impact of spreading the aim points on operational performance is also evaluated. The cumulative slew time of the heliostats from standby position to the receiver were recorded for each aiming strategy and used to determine the impact on a proxy start-up time. An increase in slew times and proxy start-up times reduced the simulated annual energy production in the System Advisor Model. Results showed that increasing the radial distance of the aim points to 150 m and higher showed a notable decrease in the simulated annual energy. Spreading the aim points to 150 m yielded an 11% reduction, while spreading the aim points to 250 m reduced the annual energy production by 23% relative to that of the baseline. It should be emphasized that the use of a proxy

startup time is a simplified and approximate method to compare the relative impact of alternative standby aiming strategies on annual energy production, and it should not be interpreted as an accurate prediction of the absolute annual energy production. Strategies to bring the heliostat beams from standby position to the receiver target sequentially rather than all at once may alleviate negative impacts of long slew times. For example, when more energy is required on the receiver, the heliostats that are aimed closest to the receiver are used first, and the heliostats that are aimed further away are brought successively toward the receiver.

Additional aiming strategies that consider the impact of glare and the direction and timing of air-traffic patterns should also be considered. Bird deterrents, their effectiveness, and the use of flux/glare shields should also be considered to further reduce environmental hazards associated with high flux and glare from concentrating solar power plants.

4. VALIDATION STUDIES

Helicopter flyovers of the National Solar Thermal Test Facility (NSTTF) at Sandia in Albuquerque, NM, and the Ivanpah Solar Electric Generating System in California were performed to validate the alternative heliostat aiming strategies and the optical tools.

4.1. Helicopter Flyover of NSTTF

A helicopter flyover of the NSTTF was performed on February 26, 2018, to assess several heliostat standby aiming strategies simulated in Section 3.2.2 (Figure 22). The flyover of the NSTTF originated from Mountain Air Helicopters in Los Lunas, NM, and proceeded to the NSTTF, where photographs were taken of the heliostat field at different locations to the south of the field (denoted by the yellow triangle in Figure 23). Data collected included the raw digital images of the glare, time, number of filters used, latitude, longitude, altitude, and DNI for three heliostat standby aiming strategies:

1. Single aimpoint: All heliostats reflect sunlight 20 m to the east and 20 m above the top of the tower
2. Dual aimpoint: Every other heliostat in a row reflects sunlight either 20 m to the east or west of the top of the tower and 20 m above
3. Up-aiming: All heliostat reflect the light straight up

After the data were collected, the images were processed using the PHLUX method to determine the irradiance at various locations [50]. The measured irradiance values were compared to predicted values using an analytical solution [29], TIM [34], and SolTrace [32].



Figure 22. Helicopter flyover of the NSTTF. Left: Julius Yellowhair (Sandia), Cliff Ho (Sandia), and Shawn Mease (Mountain Air Helicopters). Right: Ready for takeoff.

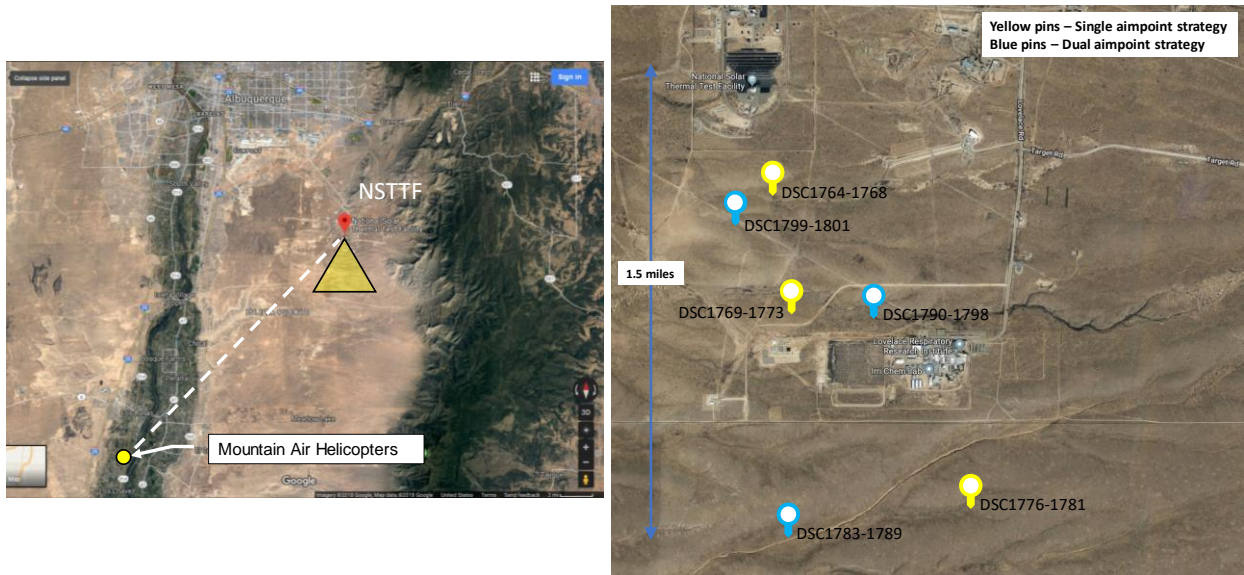


Figure 23. Left: Route from Mountain Air Helicopters in Los Lunas to the NSTTF on KAFB. Right: locations of photographs for irradiance calculations at altitudes from ~1000 feet to ~4000 feet above ground level.

Figure 24 and Figure 25 show views of the observed glare for the single aimpoint and dual aimpoint strategies, respectively. Glare from the single aimpoint strategy originates from a single location in the heliostat field, depending on the observer location. Glare from the dual aimpoint strategy originates from two points in the heliostat field since the heliostats are reflecting light to both sides of the top of the tower.



Figure 24. Views of glare at short, medium, and long observation distances using a single aimpoint strategy (20 m to the east (right) and 20 m above the top of the tower).

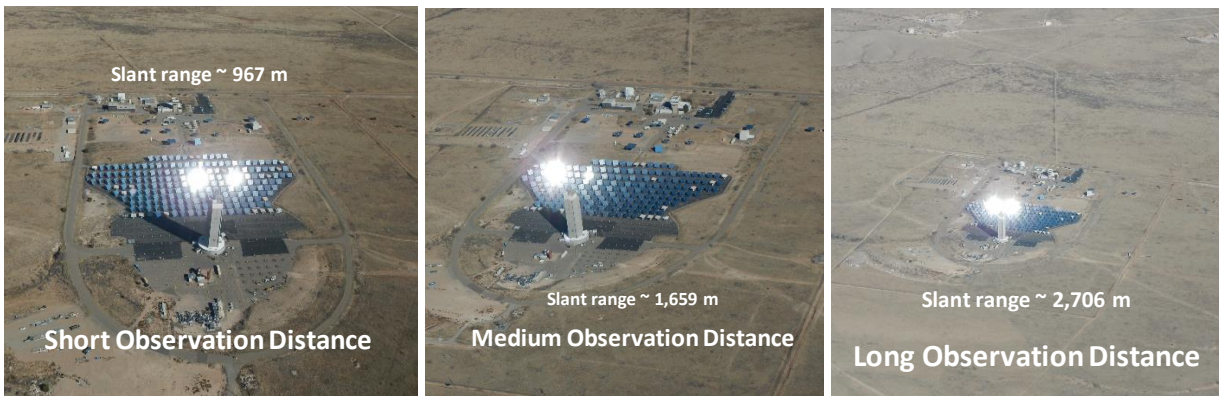


Figure 25. Views of glare at short, medium, and long observation distances using a dual aimpoint strategy (20 m to the west and east of the top of the tower and 20 m above).

Figure 26 shows two sequential images. The first is an image of glare observed during the dual aimpoint strategy. The second is an image taken shortly afterwards when the heliostats were moved to an up-aiming strategy. No glare was visible until we positioned the helicopter directly over the heliostats. Even then, we had to lean out of the helicopter to look straight down to observe glare from the heliostats. With limited downward viewing angles, pilots and passengers would typically not be able to see glare if up-aiming strategies were used. In fact, since the downward viewing angle for pilots is typically limited to less than 30 degrees from the cockpit [51], heliostats could be aimed within a 60 degree cone angle from zenith (90 degrees – 30 degrees) and still not be visible to pilots during normal flying conditions. This could aid in mitigating glare while minimizing slew time back to the receiver.



Figure 26. Views of conventional standby aiming (dual aimpoint) (left) and up-aiming strategy (right).

Figure 27 and Figure 28 show images of TIM and SolTrace simulations of glare, respectively, for the single aimpoint strategy at different distances. The distances and locations correspond to the distances and locations of the observed glare in the photographs in Figure 24. Note that the distance reported in the TIM simulations is the distance between the observer and the base of the tower. Since the glare source is near the middle of the heliostat field, which is $\sim 100 - 150$ m away from the tower, the location of the observer in the TIM simulations was chosen to be about $100 - 150$ m short of the observed distance in the photographs.

The corneal and retinal irradiances, subtended glare angle, and ocular impact are shown in the TIM simulations. At the closest distance, the TIM simulations show that the ocular impact is “yellow,” meaning that there is a strong potential for after-image. At further distances, the ocular impact becomes “green,” which denotes a minimal potential for ocular impact. Actual observations from the crew of the helicopter confirmed this finding.

The simulated irradiances from TIM and SolTrace and the analytical irradiances [29] are plotted in Figure 29 as a function of distance, together with the measured values from the flyover. The simulated irradiances are also plotted against the measured values in a parity plot shown in Figure 30. Results show that the simulations and analytical solution consistently overpredict the measured irradiance values. The SolTrace simulation results are similar to the analytical results and yield the greatest overprediction. The slope of the parity plot between SolTrace and the measured results shows that SolTrace overpredicts the measured irradiance by a factor of ~ 2.7 . TIM overpredicts the measured values by a factor of ~ 1.7 .

A potential reason for the discrepancy is the spatially discrete (rather than continuous) nature of the glare. Figure 31 shows filtered images of the glare, which reveal that the source of the glare originates from individual facets (or parts of facets). Gaps in between facets or heliostats do not reflect the sunlight. The analytical model assumes a continuous source (and size) of the glare based on the subtended glare angle (determined by the sun angle and prescribed slope error of the mirrors) and distance between the observer and glare source. TIM and SolTrace model the individual heliostats, but the heliostat is assumed to be a single continuous reflective surface. Thus,

the simulated and analytical values for irradiance are expected to overpredict the measured irradiance, which is conservative.

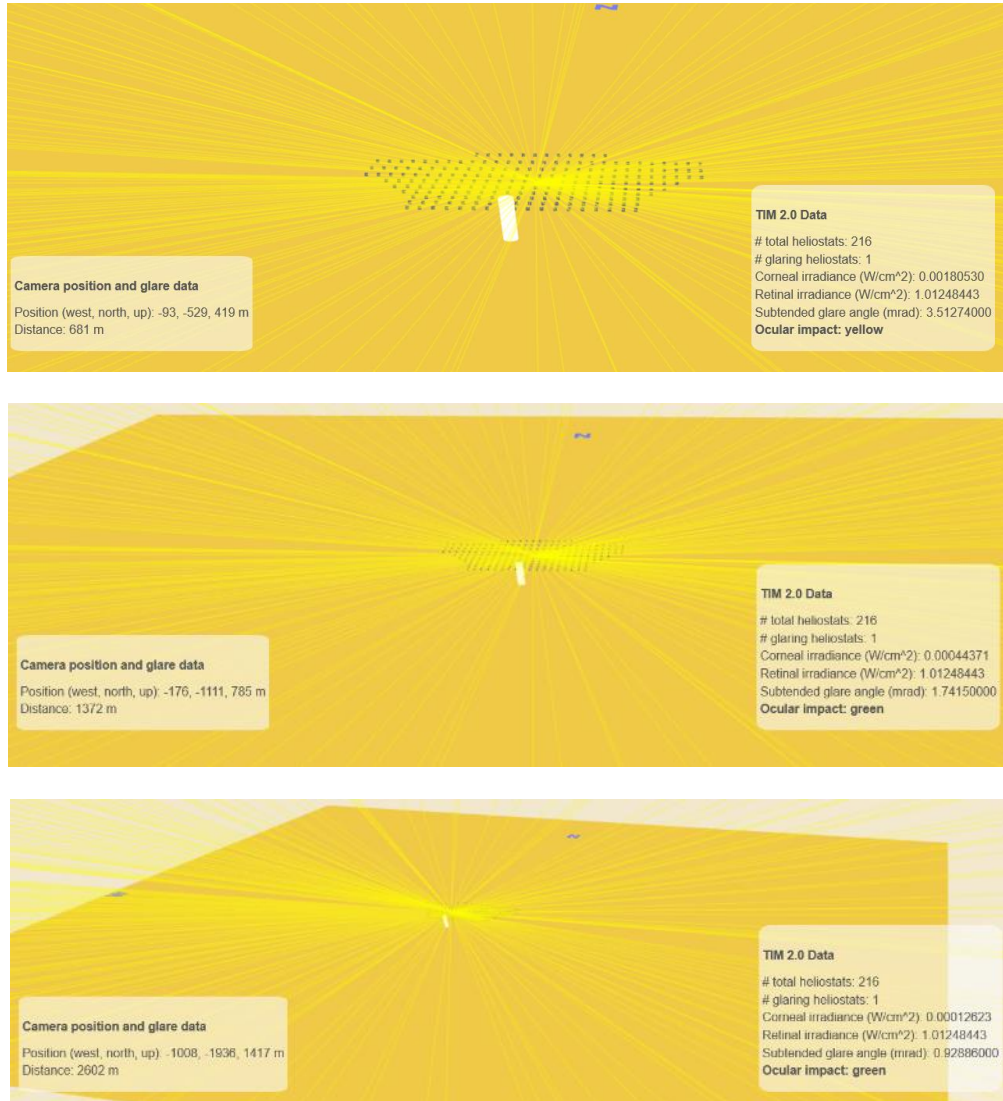


Figure 27. TIM simulations of glare from the NSTTF (single aimpoint) at the short, medium, and long observation distances.

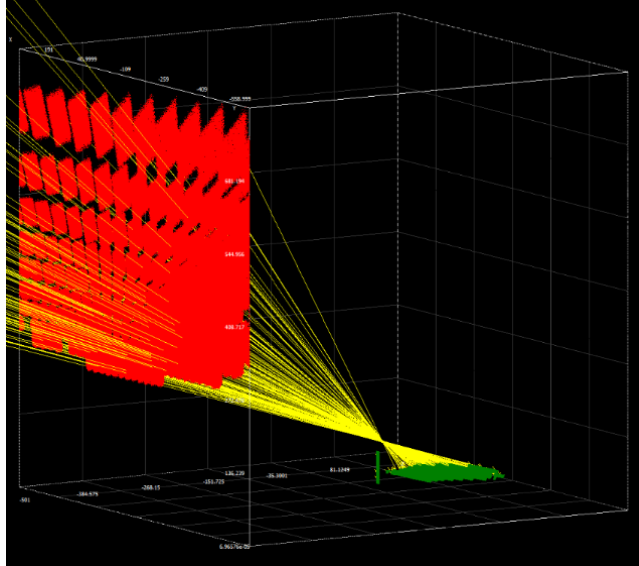


Figure 28. SolTrace simulation of a single aimpoint strategy at the NSTTF.

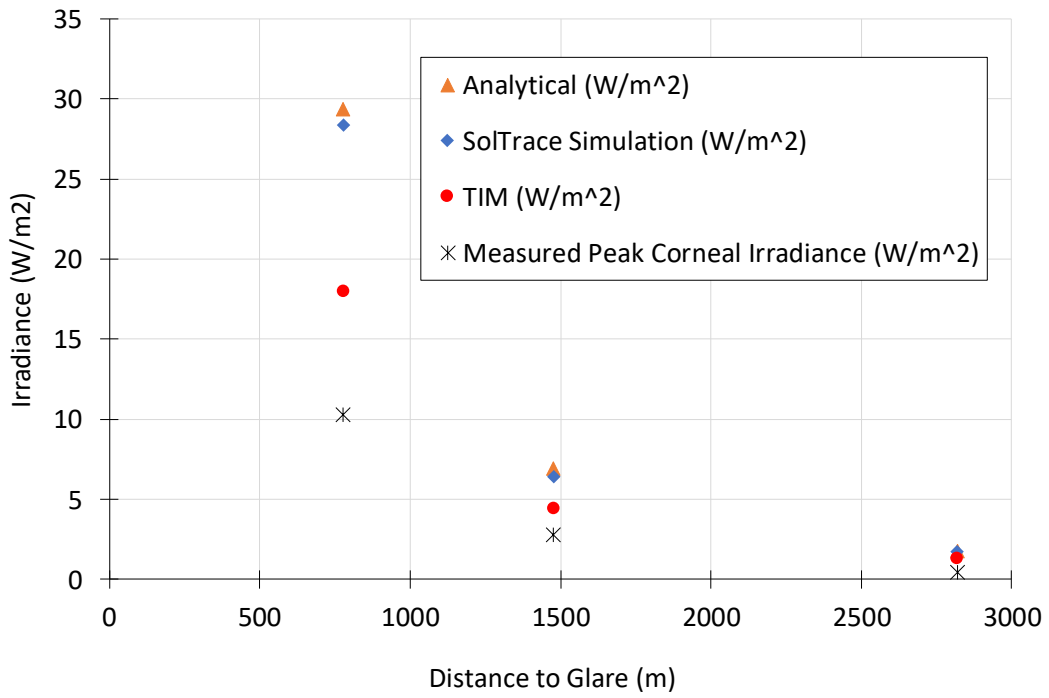


Figure 29. Measured and predicted corneal irradiance as a function of distance to glare source at the NSTTF.

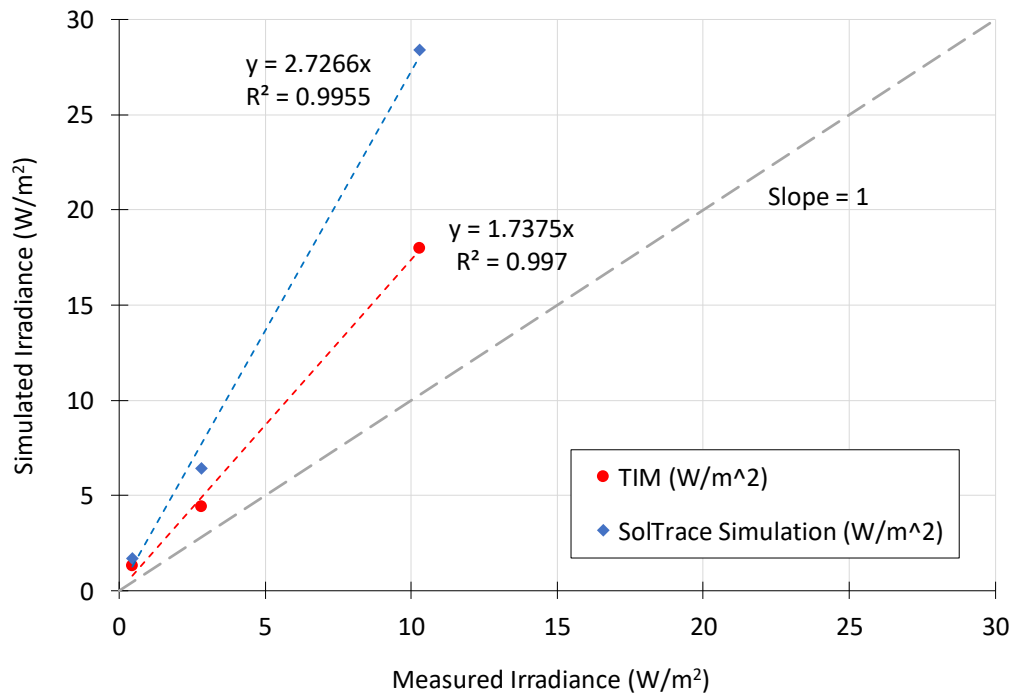


Figure 30. Parity plot of simulated irradiance vs. measured irradiance at the NSTTF.

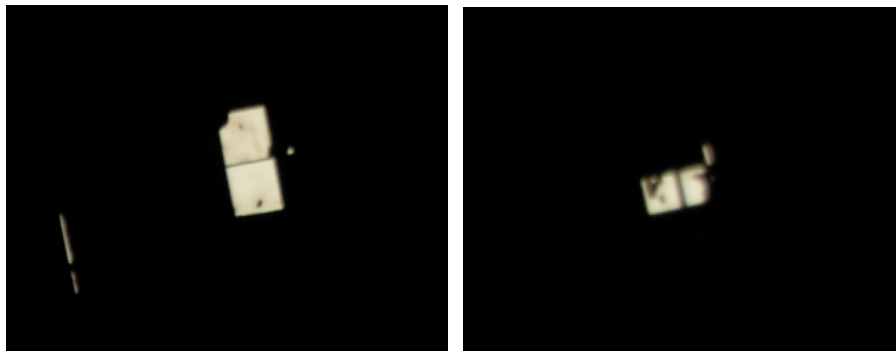


Figure 31. Filtered images of heliostat glare showing reflections from individual facets.

4.2. Helicopter Flyover of Ivanpah Solar Electric Generating System

A second helicopter flyover was conducted on May 24, 2018, over the Ivanpah Solar Electric Generating System (ISEGS). Previous flyovers had been conducted at Ivanpah in April 2014, July 2014, and March 2015. The California Energy Commission also conducted two flyovers of Ivanpah in May 2014 and April 2015. The purpose of the current flyover was to evaluate current glare conditions relative to previous flyovers and to provide data for model validation.

4.2.1. Summary of Previous and Current Flyovers

A summary of findings from the flyovers is provided below:

- **April 24, 2014 – Sandia National Laboratories**
 - Heliostats in standby mode can cause glare to aerial observers
 - Glare from heliostats can cause after-image at far distances (up to 6 miles in our helicopter surveys); similar to briefly looking at sun
 - Glare was visible from multiple heliostats in standby mode
 - The glare from the illuminated receiver was small compared to the glare from the standby heliostats
 - Ground-based drive-by surveys did not reveal ocular hazards
- **May 8, 2014 – CEC Staff and Contractors**
 - Observed glare from “direct solar reflections from the heliostats (DSRH)” in standby mode that were sufficient to result in “disability glare” that can compromise visual performance and flight safety
- **July 22, 2014 – Sandia National Laboratories**
 - Glare was still bright, but more dispersed
 - Ocular hazard was near the threshold for after-image
- **March 23, 2015 – Sandia National Laboratories**
 - Glare was still bright, about the same as July 22, 2014
 - Unit 2 had a late start (technical difficulties), so more heliostats were on standby during our flyover between ~8:30 – 9:30 AM
 - Glare was noticeably brighter from Unit 2 during most of our flyover
 - Pilot (Naomi Jacobs) stated that the glare was a distraction (at worst), but it was not a problem for her
 - She would not characterize the glare as a hazard
 - She said she could read her instruments after viewing the glare (with sunglasses) and scan for other aircraft in the direction of the glare
- **April 17, 2015 – CEC Staff and Contractors**
 - Gregg Irvin, CEC contractor
 - “All 3 towers the same, disability glare events noticeably reduced in magnitude and frequency, additional mitigation required, the number of heliostats required to produce a disability glare event (in relatively close spatial proximity) is quite low.”
 - Gary Cathey, Pilot (California Department of Transportation)
 - “I observed that the facility was exceedingly bright, to the point that I had to turn my head away from the facility to avoid the intense glare. It was difficult to scan the sky for aircraft that may have been in the area between me and ISEGS (or potentially behind ISEGS from my perspective) as we orbited the facility. As previously stated, the facility is the brightest man-made, glare producing, series of closely spaced reflective objects I have observed while flying.”
- **May 24, 2018 (current flyover) – Sandia National Laboratories**
 - The persistence and intensity of the glare was less than that of previous flyovers
 - We actually had a hard time finding a location where the glare was persistent. Glare would appear from a single heliostat (which was very bright), but then quickly

- disappear as we slowly traversed the airspace in the helicopter. During previous flyovers, the glare was much more persistent as we traversed the airspace.
- Reduction in perceived glare was attributed to standby aiming strategy
 - Heliostats were aimed randomly to the left or right of the receiver and within a prescribed large annulus of different radii (~24 m – 90 m)
 - Previous aiming strategies included the following:
 - Aiming to one side (left side) of the receiver, as close as possible to the receiver (~25 – 60 m)
 - Aiming to both sides of the receiver, as close as possible to the receiver

Suggested mitigation measured from the previous studies included the following:

- Limit the number of heliostats in standby mode
 - Predict need for standby heliostats based on cloud cover or other factors
 - Bring heliostats up to standby position near receiver sequentially only as needed
- Implement dynamic aiming strategy and reflect light either straight up or toward the ground (depending on heliostat location and slew time to target)
- Increase the number of aim points near the receiver during standby and have adjacent heliostats point to different locations to disperse visible glare (implemented)
- Reduce number of standby heliostats that face directly toward the sun; these produce the most glare
- Incorporate a glare shield near the receiver for heliostats in standby mode
 - Perhaps the shield can serve as a preheater
- Improve tracking and positioning algorithms to reduce the number of “rogue” heliostats

Figure 32 shows a sequence of aerial photos of glare taken during helicopter flyovers at Ivanpah on different dates. The initial flyover on April 24, 2014, shows visible glare that was clustered close to the receiver, which is consistent with the original standby aiming strategy to point the heliostats as close to the receiver as possible. The photos during subsequent flyovers on July 22, 2014, and March 23, 2015, show that the glare from the heliostats was spread further apart, consistent with a change in aiming strategy to spread the aim points to locations further from the receiver. On May 24, 2018, the glare is not as intense or spread out.



Figure 32. Sequence of photos of glare at Ivanpah taken on different dates looking northwest. Note that on May 24, 2018, Unit 1 was not operational.

4.2.2. Evaluation of Current Flyover of Ivanpah

With regard to the most recent flyover of Ivanpah on May 24, 2018, photographs of glare from Units 2 & 3 (Unit 1 was not operational) were analyzed using the PHLUX tool [50] for corneal and retinal irradiances, subtended glare angles, and potential ocular hazard. In addition, TIM and SolTrace simulations of the glare at Ivanpah were performed and compared to the measured irradiances.

The helicopter flyover of Ivanpah on May 24, 2018, was performed by the Mission Test and Support Services out of Nellis Air Force Base in Nevada (Figure 33). The flight departed from the Henderson Executive Airport at ~11 AM and arrived at Ivanpah ~11:30 AM. Photographs of the glare were taken at various locations around the Ivanpah plant from ~11:30 AM – 12:30 PM (Figure 34). The locations were similar to locations where photographs were taken during previous flyovers by Sandia. The time of day was chosen to coincide with the most number of heliostats in standby position.



Figure 33. From left to right: Carl Maassberg (NRG), Cliff Ho (Sandia), and Mike Toland (Mission Support & Test Services, Nellis AFB) prior to flyover of Ivanpah on May 24, 2018.

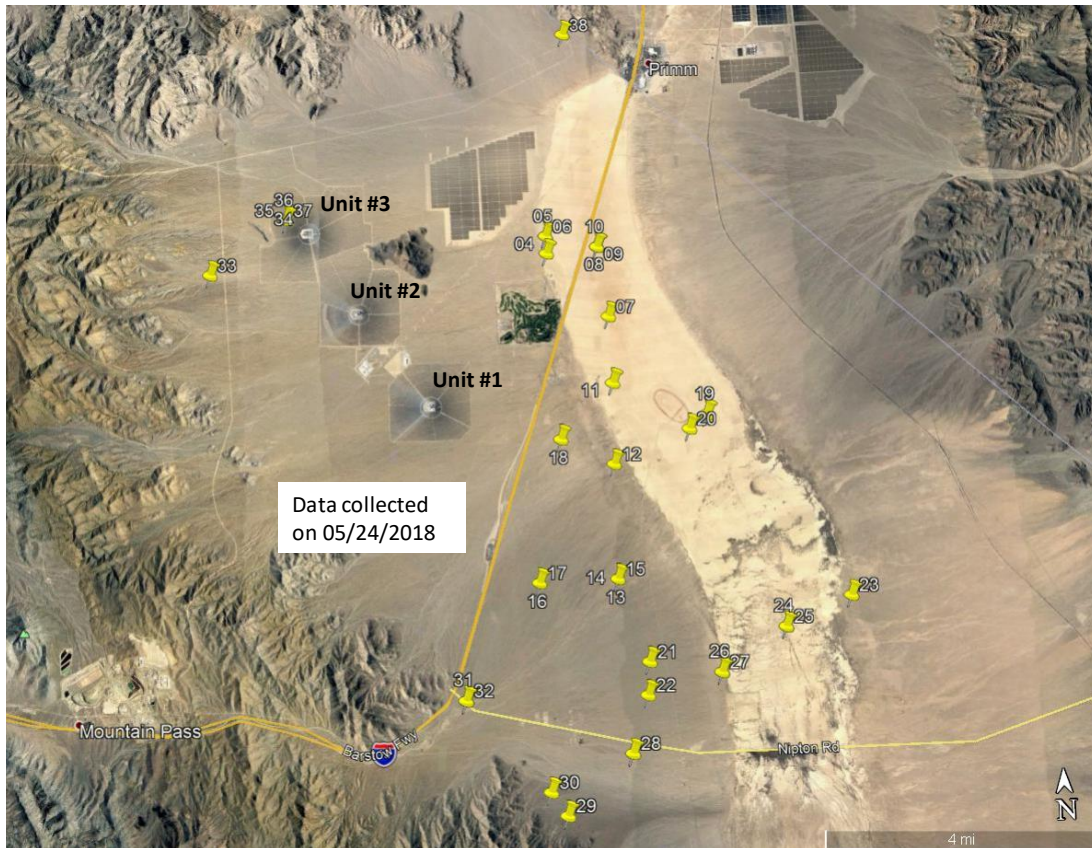


Figure 34. Locations of photographs taken on May 24, 2018.

Figure 35 shows representative photographs of glare observed during the flyover from different locations. In general, the glare was less persistent and less intense than during previous flyovers. We believe that the aiming strategy that reflects the light to both sides of the receiver randomly within a large annulus of different radii helped reduced the persistence and magnitude of the glare.



Figure 35. Left: Looking northwest at Units 2 and 3. Right: Looking southeast at Units 3, 2, and 1 (Unit 1 was not operational).

Figure 36 shows additional photos of the glare, as well as filtered images that show that the source of glare was typically from individual facets of a heliostat. During previous flyovers, glare from well-defined clusters of heliostats was often visible, and the glare translated along the heliostat field as we flew over the heliostats. During the current flyover, it appeared that the glare was from individual heliostats, and the glare did not translate across the heliostat field in a regular or persistent fashion.



Figure 36. Photos of glare at Ivanpah (top) and filtered images (bottom) revealing glare from individual facets. The intensity of the glare was notably less than previous flyovers.

Figure 37 shows simulations of the glare at Ivanpah Unit 2 using SolTrace and TIM. Because of the large number of heliostats (over 50,000), SolTrace required a large number of rays (we used 55 million rays) and long simulation times (many hours). We believe that the simulation of irradiance at specific locations in the airspace may not be accurately represented since the simulated SolTrace irradiance was less than the analytical and TIM results. In the comparisons of the NSTTF flyover, the SolTrace results yielded higher irradiances than TIM that were close to the analytical solution.

Similar to the results of the NSTTF flyover, the measured irradiance values are generally lower than the TIM results at all distances, and considerably lower than the analytical results (

Figure 38). This is due to the discrete nature of the glare from the heliostat facets versus the assumed continuous region of glare in the analytical model. The simulated values of irradiance using TIM better match the measured results for long distances (> ~12 km) relative to shorter distances, and all results show a general trend of decreasing irradiance with increasing distance. However, the measured and simulated (TIM and SolTrace) results are strongly variable.

Figure 39 shows the parity plot between the simulated and measured irradiances. Results show that there is a lack of correlation between the simulated and measured values. The measured values exhibited strongly varying magnitudes due to the limited amount of glare visible in any image and the relative position of the heliostats. In some cases, the glare would be captured by the heliostat facets; in other cases, the glare would be missed by gaps in the heliostats. The simulated values were also variable due to the reasons discussed above.

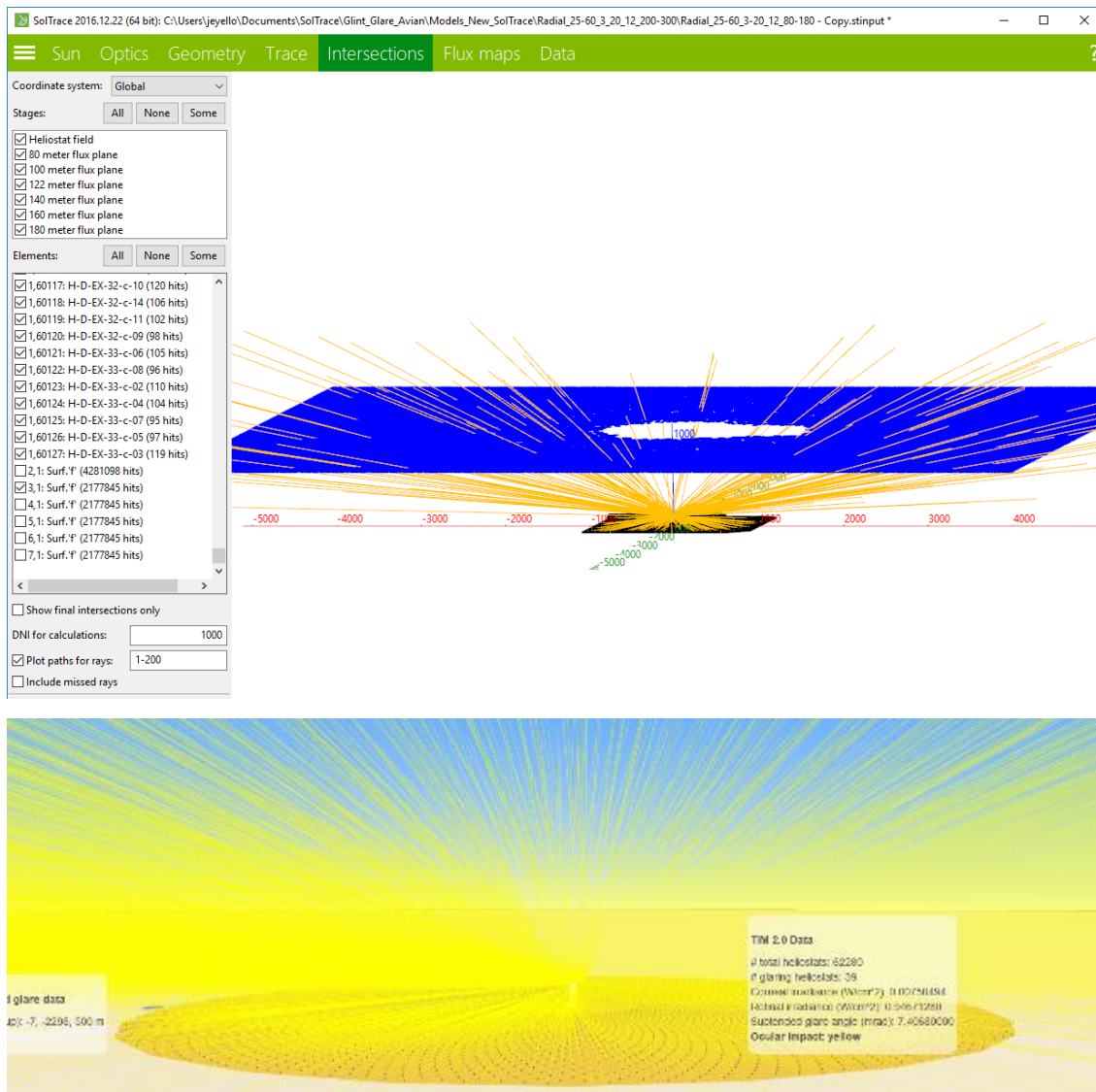


Figure 37. Simulations of irradiance at Ivanpah (Unit 2) using SolTrace (top) and TIM (bottom).

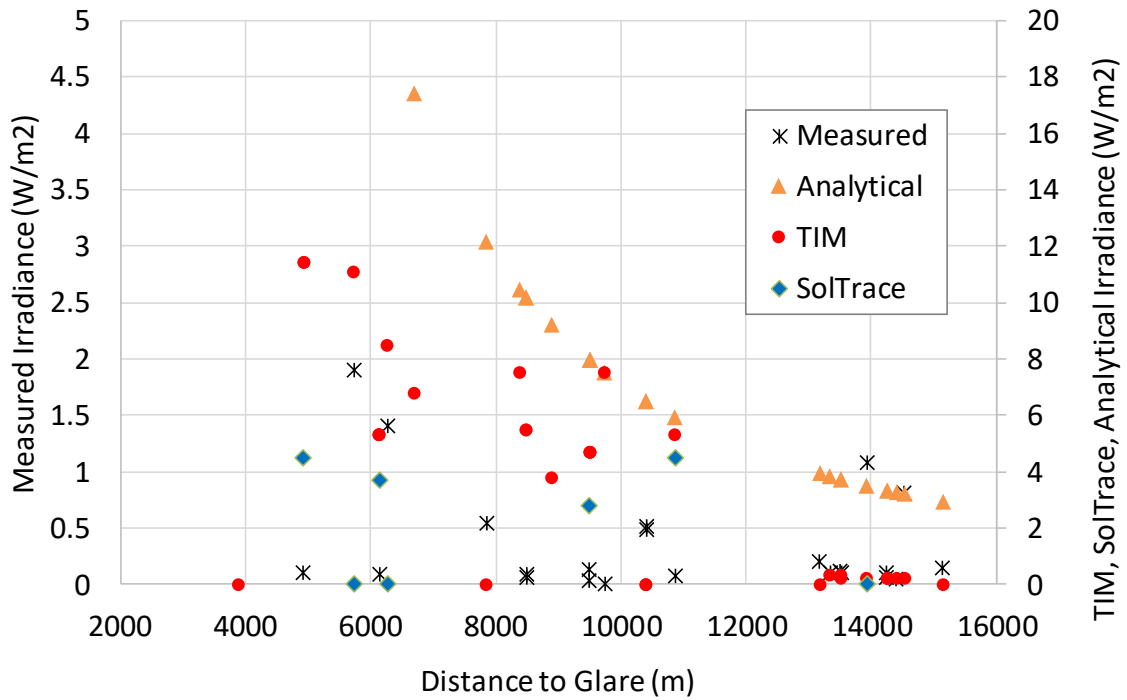


Figure 38. Measured and predicted corneal irradiance as a function of distance to glare source at Ivanpah.

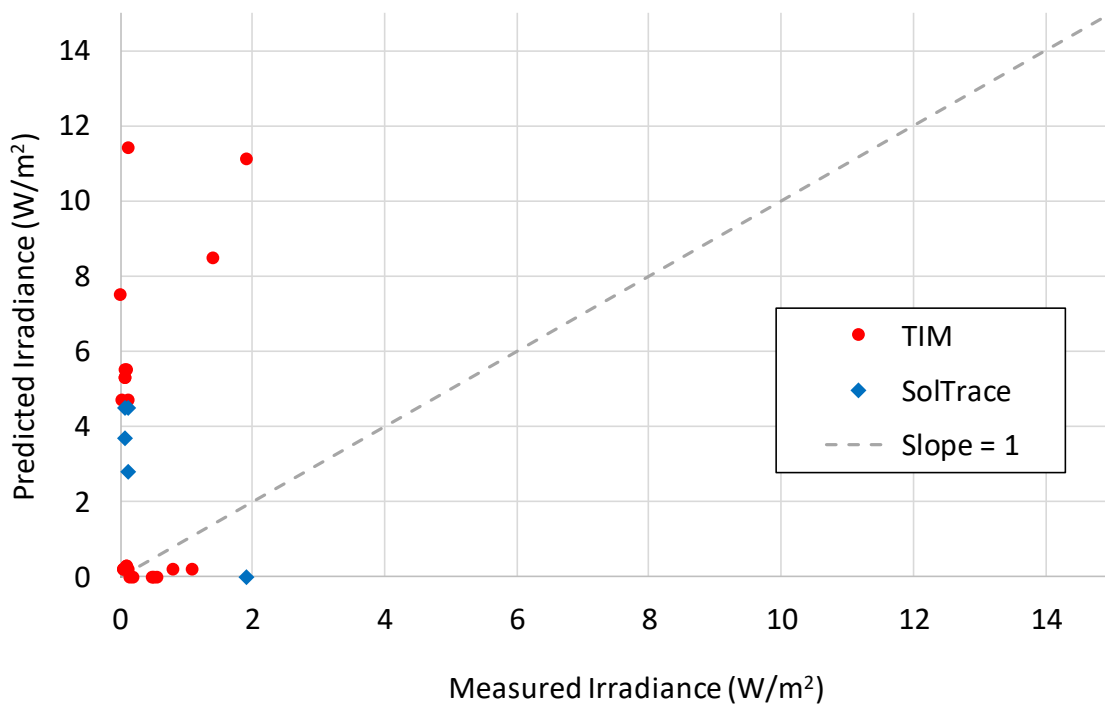


Figure 39. Parity plot of simulated irradiance vs. measured irradiance at Ivanpah.

Figure 40 shows the ocular hazard plot for the images taken during the May 24, 2018, flyover of Ivanpah. Results showed that all of the images yielded a low potential for after-image.

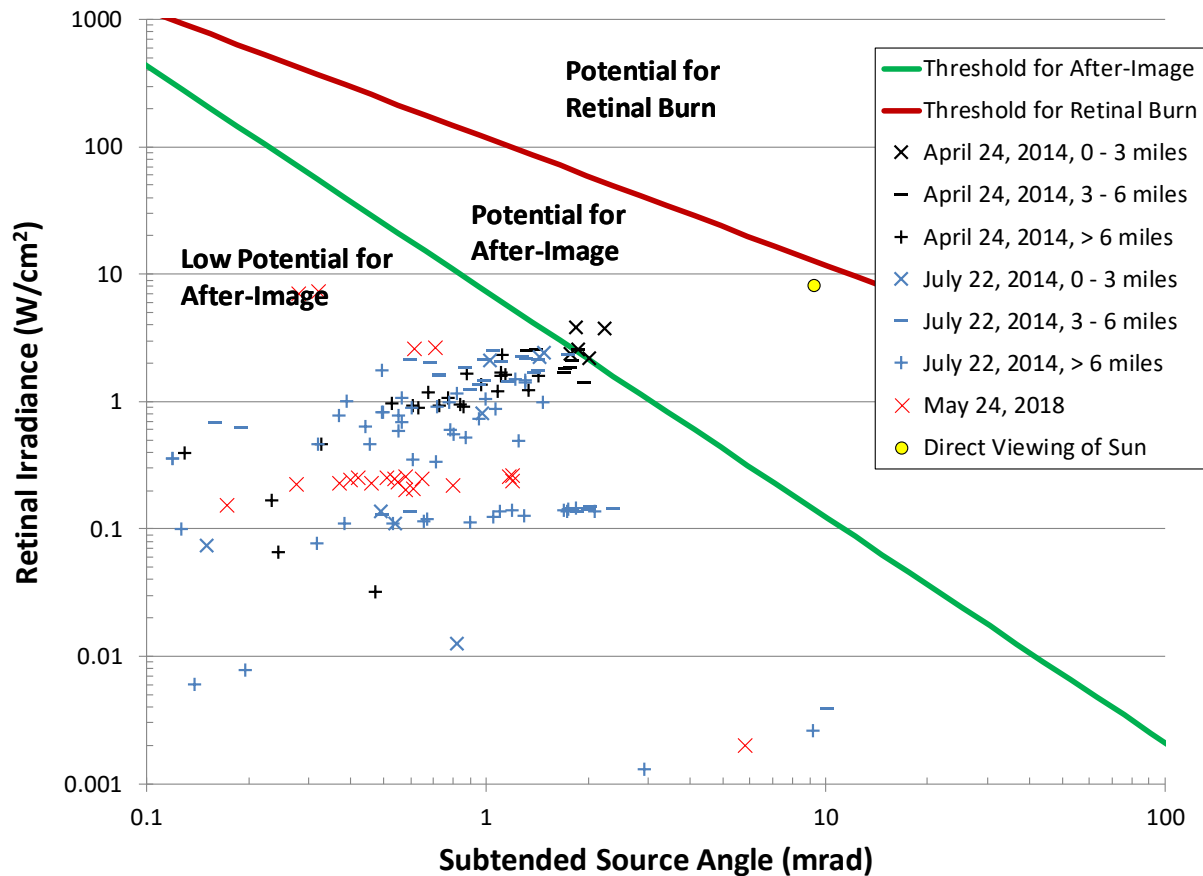


Figure 40. Ocular hazard plot for glare observed during flyover at Ivanpah between 2014 and 2018. All images yielded a low potential for ocular impact. The yellow dot indicates direct viewing of the sun.

4.3. Summary

Two helicopter flyovers were conducted during this study at the NSTTF and at the Ivanpah Solar Electric Generating System. Three heliostat aiming strategies were evaluated at the NSTTF: (1) single aimpoint, (2) dual aimpoint, and (3) up-aiming. Results showed that the up-aiming strategy can mitigate visible glare to pilots due to the limited downward viewing angle from the cockpit. Comparisons between the simulated and measured irradiances at various locations in the airspace showed that the measured irradiance was consistently less than the SolTrace or TIM-simulated values due to the limited, discrete reflective area of the heliostat facets. The predicted and measured results all showed similar trends of decreasing irradiances as a function of distance.

The flyover of Ivanpah revealed that the observed glare was less persistent and less intense than during previous flyovers. This was attributed to an aiming strategy that randomly spread the aimpoints to both sides of the receiver within a large annulus of varying radii. This resulted in observable glare that originated from individual heliostats rather than clusters of heliostats. Models of the ocular hazard yielded a low potential for after-image. Simulations of the glare using SolTrace were difficult due to the large number of rays required, and there was a lack of correlation with the measured values. TIM results also lacked a clear correlation with the measured values, partly because of the aiming strategy that limited the glare area from individual heliostats and caused strongly varying irradiance values. However, the TIM simulations and analytical values showed generally similar trends of decreasing irradiances with increasing distances.

5. CONCLUSIONS

5.1. Glare Hazard Analyses

Glare from solar energy installations can pose potential hazards for pilots and motorists. SGHAT and ForgeSolar are tools that can be used to evaluate potential glare from PV arrays and alternative designs that can mitigate glare while maximizing energy production. The current work has developed several enhancements to SGHAT, including block-space receptor models, integration of PVWatts, and a 3D daily glare visualization feature. SGHAT technology has been licensed to Sims Industries, which released the ForgeSolar suite of glare analysis tools. Ray-tracing tools such as SolTrace provide more rigorous optical analyses for both PV and CSP systems, but they are computationally more expensive. A fast interactive tool called TIM (Tower Illuminance Model) has been developed as part of the current work that allows glare analyses from various heliostat field configurations for CSP. The user can “fly” through the airspace to determine the irradiance and potential ocular hazards at any location.

5.2. Flux Hazard Analyses

CSP plants with heliostat fields can create high-flux regions in the airspace that can singe birds. This work has presented a study of alternative heliostat standby aiming strategies and their impact on avian exposure hazards. A model was developed to assess the bird-feather temperature as a function of solar irradiance, thermal emittance, and convection as the bird flies through the airspace above the heliostat field. Different heliostat aiming strategies were evaluated, and results showed that spreading the radial aim points reduced the cumulative time that feather temperatures exceeded the hazard metric of 160 °C.

However, spreading the aim points increased the cumulative slew time of the heliostats from standby position to the receiver. An increase in slew times and proxy start-up times reduced the simulated annual energy production in the System Advisor Model. Strategies to bring the heliostat beams from standby position to the receiver target faster, perhaps sequentially rather than all at once, may alleviate negative impacts of long slew times.

5.3. Validation

TIM and SolTrace tended to overestimate the irradiance and potential glare at the NSTTF due to the measured values being limited to individual facets and not from continuous reflective surfaces. Analytical models also overpredicted the irradiance, but the trend between the simulations,

analytical results, and measured values were consistent and showed decreasing irradiances with increasing distances. At Ivanpah, the amount of glare was noticeably less than during previous flyovers. Glare was not continuous due to the bi-directional and random aiming scheme around the receiver.

5.4. Recommendations

Tools such as SGHAT and ForgeSolar should be used to evaluate potential glare hazards from PV arrays and to identify designs that both mitigate glare and maximize energy production. A new tool, TIM, can be used to evaluate glare and avian hazards from CSP power tower systems using alternative heliostat standby aiming strategies. To avoid both glare and avian-flux hazards, we recommend an up-aiming strategy during heliostat standby conditions (Figure 41). The flyover of the NSTTF demonstrated that the up-aiming strategy alleviates glare, and it can also reduce flux hazards to birds as well by limiting the flux to one sun in the airspace above the heliostat field during standby conditions. A staged heliostat standby scheme should be developed to minimize the heliostat slew times and impacts on start-up and operation. Finally, there are three factors to be considered in selecting an optimal standby aiming strategy: (1) glare, (2) avian flux hazards, and (3) plant operation. Future studies should consider the trade-offs and collective impacts on all three factors.

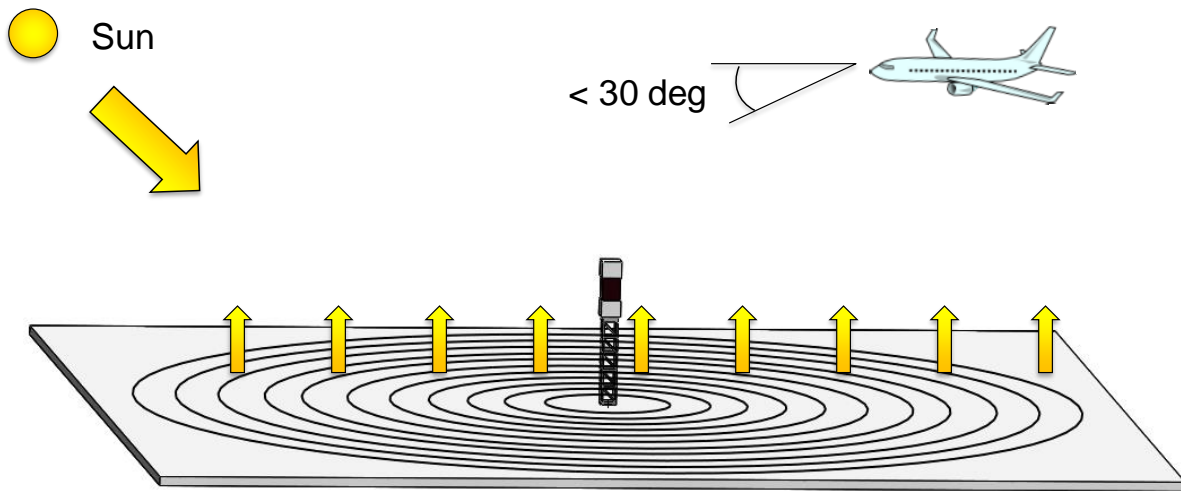


Figure 41. Up-aiming strategy can alleviate both glare and avian hazards, but heliostat slew times back to the receiver may be increased.

REFERENCES

- [1] Barrett, S., P. Devita, and C. Ho, 2014, Energy Technologies' Compatibility with Airports and Airspace: Guidance for Aviation and Energy Planners, *J. Airport Management*, **8**(4), p. 318-326.
- [2] Barrett, S.B., P.M. DeVita, L.R. Lambert, C.K. Ho, B. Miller, Y. Zhang, and M. Vigilante, 2014, Guidebook for Energy Facilities Compatibility with Airports and Airspace, Airport Cooperative Research Program Report 108, Washington, D.C.. 94 pp.
- [3] California Energy Commission, Letter re Pilot Complaints of Visual Impacts from Ivanpah Solar Electric Generating System, Docket #07-AFC-05C, TN #201847, March 10, 2014, <http://www.energy.ca.gov/sitingcases/ivanpah/>.
- [4] CNN, 2012, Solar Panels Cause Trouble at Airport, Heather Hamel reporting, WMUR, August 30, 2012., http://www.cnn.com/video/standard.html?hpt=hp_t3#/video/bestoftv/2012/09/01/nh-dnt-airport-solar-panels-safety-issues.cnn.
- [5] Federal Aviation Administration. *Interim Policy, FAA Review of Solar Energy System Projects on Federally Obligated Airports, Federal Register, Vol. 78, No. 205, 63276, October 23,*. 2013.
- [6] Jakubiec, J.A. and C.F. Reinhart, 2014, *Assessing Disability Glare Potential Due to Reflections from new Constructions: A Case Study Analysis and Recommendations for the Future*, in *2014 Transportation Research Board 93rd Annual Meeting*, Washington, D.C., January 12 - 16, 2014.
- [7] U.S. Department of Energy EERE Website. *Examples of Codes that Address Glare from Solar Energy Systems*. 2012 July 30, 2012; Available from: http://www4.eere.energy.gov/solar/sunshot/resource_center/ask/question/question_11.
- [8] Wybo, J.L., 2013, Large-scale photovoltaic systems in airports areas: safety concerns, *Renewable and Sustainable Energy Reviews*, **21**, p. 402-410.
- [9] California Energy Commission. *Ivanpah Solar Electric Generating System (Compliance), Docket Number 07-AFC-05C*. 2014 12/3/14; Available from: http://docketpublic.energy.ca.gov/PublicDocuments/07-AFC-05C/TN203395_20141203T090345_IVANPAH_SOLAR_GENERATING_SYSTEM_GLARE_INVESTIGATION.pdf.
- [10] California Energy Commission. *Joint Workshop for the Rio Mesa Solar Electric Generating Facility (2011-AFC-04) and Hidden Hills Solar Electric Generating System (11-AFC-02)*. 2012 9/17/2012; Available from: http://www.energy.ca.gov/sitingcases/riomesa/documents/2012-08-28_joint_workshop/.
- [11] L.J. Walston et al., 2015, A Review of Avian Monitoring and Mitigation Information at Existing Utility-Scale Solar Facilities, Argonne National Laboratory, Environmental Science Division, ANL/EVS-15/2, prepared for the U.S. Department of Energy.
- [12] McCrary, M.D., R.L. McKernan, P.A. Flanagan, and W.D. Wagner, 1984, *Wildlife Interactions at Solar One: Final Report*, Prepared for Southern California Edison Company, Rosemead, CA, Los Angeles County Natural History Museum Foundation, Section of Ornithology, Los Angeles, CA.
- [13] Sovacool, B.K., 2013, The avian benefits of wind energy: A 2009 update, *Renewable Energy*, **49**, p. 19-24.

- [14] New Hampshire Union Leader. *Almost \$2M to Correct Out-of-Position Airport Solar Panels*. 2014 2/14/14; Available from: <http://www.unionleader.com/article/20140215/NEWS05/140219416/1013>.
- [15] Office of the Under Secretary of Defense, Memorandum for Assistant Secretary of the Army (Installations, Environment, and Energy) Assistant Secretary of the Navy (Energy, Installations, and Environment) Acting Assistant Secretary of the Air Force (Installations, Environment and Logistics) - Subject: "Glint/Glare Issues on or near Department of Defense (DoD) Aviation Operations", Washington D.C., June 11, 2014,
- [16] U.S. Department of Defense Instruction, Air Installations Compatible Use Zones (AICUZ), DoDI 4165.57, March 12, 2015 (Change 1), May 2, 2011 (original),
- [17] Daily Republic. *Solano Board Extends Ban on Large Renewable Energy Projects*. December 4, 2013; Available from: <http://www.dailyrepublic.com/news/solanocounty/county-extends-ban-on-large-renewable-energy-projects/>.
- [18] M. Peck (IEEE Spectrum). *Ivanpah Solar Power Tower is Burning Birds*. 8/20/14; Available from: <http://spectrum.ieee.org/energywise/green-tech/solar/ivanpah-solar-plant-turns-birds-into-smoke-streamers>.
- [19] Kagan, R.A., T.C. Viner, P.W. Trail, and E.O. Espinoza, 2014, Avian Mortality at Solar Energy Facilities in Southern California: A Preliminary Analysis, National Fish and Wildlife Forensics Laboratory, <http://alternativeenergy.procon.org/sourcefiles/avian-mortality-solar-energy-ivanpah-apr-2014.pdf>,
- [20] H. T. Harvey and Associates, Ivanpah Solar Electric Generating System Avian & Bat Monitoring Plan - 2013-2014 Annual Report (Revised), Docket Number 07-AFC-05C, TN#204258, 2015, <https://efiling.energy.ca.gov/Lists/DocketLog.aspx?docketnumber=07-AFC-05C>.
- [21] Western EcoSystems Technology, I., Ivanpah Solar Electric Generating System Avian & Bat Monitoring Plan - 2014-2015 Annual Report and Two-Year Comparison 21 October 2014 – 20 October 2015, Docket Number 07-AFC-05C, TN#212042, 2016, <https://efiling.energy.ca.gov/Lists/DocketLog.aspx?docketnumber=07-AFC-05C>.
- [22] Danko, P. *More Problems for CSP: Ivanpah Solar Plant Falling Short of Expected Electricity Production*. 2014 October 30, 2014; Available from: <http://www.greentechmedia.com/articles/read/ivanpah-solar-plant-falling-short-of-expected-electricity-production>
- [23] Ho, C.K., 2016, Review of Avian Mortality Studies at Concentrating Solar Power Plants, *Solarpaces 2015: International Conference on Concentrating Solar Power and Chemical Energy Systems*, **1734**.
- [24] Mccrary, M.D., R.L. Mckernan, R.W. Schreiber, W.D. Wagner, and T.C. Sciarrotta, 1986, Avian Mortality at a Solar-Energy Power-Plant, *Journal of Field Ornithology*, **57**(2), p. 135-141.
- [25] Saur, R.L. and S.M. Dobrash, 1969, Duration of Afterimage Disability after Viewing Simulated Sun Reflections, *Applied Optics*, **8**(9), p. 1799-1801.
- [26] Sliney, D.H. and B.C. Freasier, 1973, Evaluation of Optical Radiation Hazards, *Applied Optics*, **12**(1), p. 1-24.
- [27] Nakagawara, V.B., K.J. Wood, and R.W. Montgomery, 2003, Natural Sunlight and Its Association to Aviation Accidents: Frequency and Prevention, DOT/FAA/AM-03/6, Civil Aerospace Medical Institute, Federal Aviation Administration, Oklahoma City, OK.

- [28] Osterhaus, W.K.E., 2005, Discomfort glare assessment and prevention for daylight applications in office environments, *Solar Energy*, **79**(2), p. 140-158.
- [29] Ho, C.K., C.M. Ghanbari, and R.B. Diver, 2011, Methodology to Assess Potential Glint and Glare Hazards From Concentrating Solar Power Plants: Analytical Models and Experimental Validation, *Journal of Solar Energy Engineering-Transactions of the ASME*, **133**(3).
- [30] Ho, C.K. and C.A. Sims, United States Patent US 8,841,592 B1, Solar Glare Hazard Analysis Tool on Account of Determined Points of Time, Sandia Corporation, Sep. 23, 2014.
- [31] Solar Glare Hazard Analysis Tool. 2014; Available from: www.sandia.gov/glare.
- [32] Wendelin, T., 2003, *SolTrace: A New Optical Modeling Tool for Concentrating Solar Optics*, in *Proceedings of the 2003 International Solar Energy Conference*, ISEC2003-44090, Hawaii, March 15-18, 2003.
- [33] Wagner, M.J., 2015, SolarPILOT User's Manual: A Tool for Solar Power Tower Layout and Optimization, National Renewable Energy Laboratory, Golden, CO.
- [34] Sims, C.A., C.K. Ho, L. Horstman, T. Wendelin, and J. Yellowhair, 2017, *Tower Illuminance Model (TIM): Interactive Real-Time Flyover Simulation Tool to Evaluate Glare and Avian-Flux Hazards*, in *SolarPACES 2017*, Santiago, Chile, September 26 - 29, 2017.
- [35] Ho, C.K. and J.E. Yellowhair, 2018, Glare Analyses of the DEWA IV CSP Power Tower in Dubai, UAE, Sandia National Laboratories, SAND2018-5454 (Official Use Only), Albuquerque, NM.
- [36] Vittori, J., 2015, Information Request - 2015 Avian Mortality Tracking, Memorandum to Tonopah Solar Energy, LLC, November 3, 2015
- [37] Walston et al., 2015, A Review of Avian Monitoring and Mitigation Information at Existing Utility-Scale Solar Facilities, Argonne National Laboratory, ANL/EVS-15/2, Argonne, IL.
- [38] Santolo, G., 2012, Potential for Solar Flux Impacts to Avian Species, Hidden Hills Solar Electric Generating System (HHSEGS) (11-AFC-2), Submitted to California Energy Commission. November 21, 2012
- [39] California Energy Commission (Tyler et al.), 2012, Appendix BIO1 - Biogeological Resources Risk Assessment of Avian Exposure to Concentrated Solar Radiation, Final Staff Assessment for the Hidden Hills Solar Electric Generating System Project, <http://www.energy.ca.gov/sitingcases/hiddenhills/documents/fsa/>,
- [40] Senoz, E., R.P. Wool, C.W.J. McChalicher, and C.K. Hong, 2012, Physical and chemical changes in feather keratin during pyrolysis, *Polymer Degradation and Stability*, **97**(3), p. 297-307.
- [41] Ho, C., T. Wendelin, L. Horstman, and J. Yellowhair, 2016, *A Method to Assess Flux Hazards and CSP Plants to Reduce Avian Mortality*, in *SolarPACES 2016*, Abu Dhabi, October 11 - 14, 2016.
- [42] Incropera, F.P., D.P. DeWitt, 1985, *Introduction to Heat Transfer*, John Wiley & Sons, New York.
- [43] Harvey, T.A., K.S. Bostwick, and S. Marschner, 2013, Directional reflectance and millimeter-scale feather morphology of the African Emerald Cuckoo, *Chrysococcyx cupreus*, *Journal of the Royal Society Interface*, **10**(86).

- [44] Yildiz, D., E.U. Bozkurt, and S.H. Akturks, 2009, Determination of Goose Feather Morphology by Using SEM, *Journal of Animal and Veterinary Advances*, **8**(12), p. 2650-2654.
- [45] Wolf, B.O. and G.E. Walsberg, 2000, The role of the plumage in heat transfer processes of birds, *American Zoologist*, **40**(4), p. 575-584.
- [46] Walsberg, G.E., 1988, Heat-Flow through Avian Plumages - the Relative Importance of Conduction, Convection, and Radiation, *Journal of Thermal Biology*, **13**(2), p. 89-92.
- [47] National Renewable Energy Laboratory. *System Advisor Model*. 2012; Available from: <https://sam.nrel.gov/>.
- [48] Ho, C.K., 2013, Relieving a Glaring Problem, *Solar Today*, (April 2013), p. 28 - 31.
- [49] Ho, C.K., C.A. Sims, and J.M. Christian, 2015, Evaluation of glare at the Ivanpah Solar Electric Generating System, *International Conference on Concentrating Solar Power and Chemical Energy Systems, Solarpaces 2014*, **69**, p. 1296-1305.
- [50] Ho, C.K. and S.S. Khalsa, 2012, A Photographic Flux Mapping Method for Concentrating Solar Collectors and Receivers, *Journal of Solar Energy Engineering-Transactions of the Asme*, **134**(4).
- [51] Federal Aviation Administration Advisory Circular, 1993, Pilot Compartment View Design Considerations, AC No: 25.773-1, U.S. Department of Transportation, January 8, 1993

APPENDIX A – VALIDATION OF BLOCK SPACE RECEPTOR FEATURE IN SGHAT

Purpose

This report outlines the methods and results used to validate the implementation of the Block Space, or Observation Region (“OB”), enhancement in the Solar Glare Hazard Analysis Tool. This feature is encompassed in Subtask 1.1.1:

Develop 3-dimensional block space analysis and visualization feature for predicting glare in an outlined area from a specified PV array.

Validation Metric & Success Value

The OB feature is assessed via the correlation of ocular impact between the new model and an existing validated method of glare prediction known as the “Lookback” method. The validation metric was defined as the correlation coefficient, r :

$$r = \frac{\sum(x - \bar{x})(y - \bar{y})}{\sqrt{\sum(x - \bar{x})^2 \sum(y - \bar{y})^2}}$$

Where x is the calculated ocular impact values at 250 sampled locations/times and y is data from the existing glare analysis method. Successful validation requires a success value of $r > 0.95$.

The process of validation was as follows:

1. Perform glare analysis on block space region. Analysis yields predicted annual glare in that region.
2. Generate 250 discrete observation points within OB.
3. Analyze every point using Lookback method.
4. Aggregate and bin OP results based on day of year and ocular impact of glare.
5. Compare OB and OP results using scatter plot
6. Derive correlation coefficient using linear regression

Validation

Three locations were selected for analysis and validation: Manchester Boston Airport (MHT), Indianapolis International Airport (IND), and Cape Town International Airport (CPT). Each site configuration included one photovoltaic array and one outlined block space region. The CPT site was selected due to its location in the southern hemisphere to ensure that the OB feature provides accurate results worldwide.

Boston Manchester Airport

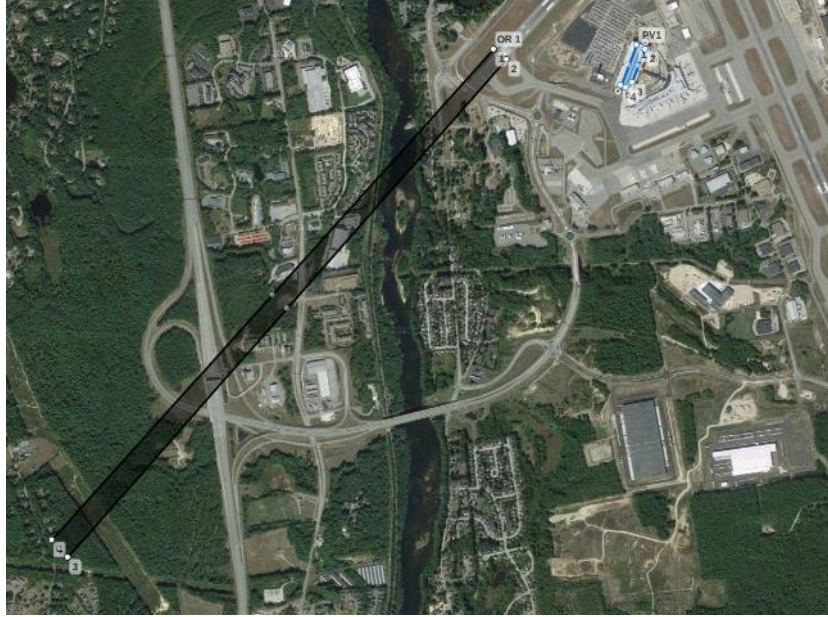


Figure 42. MHT block space (grey) and PV array (blue) in map editor.

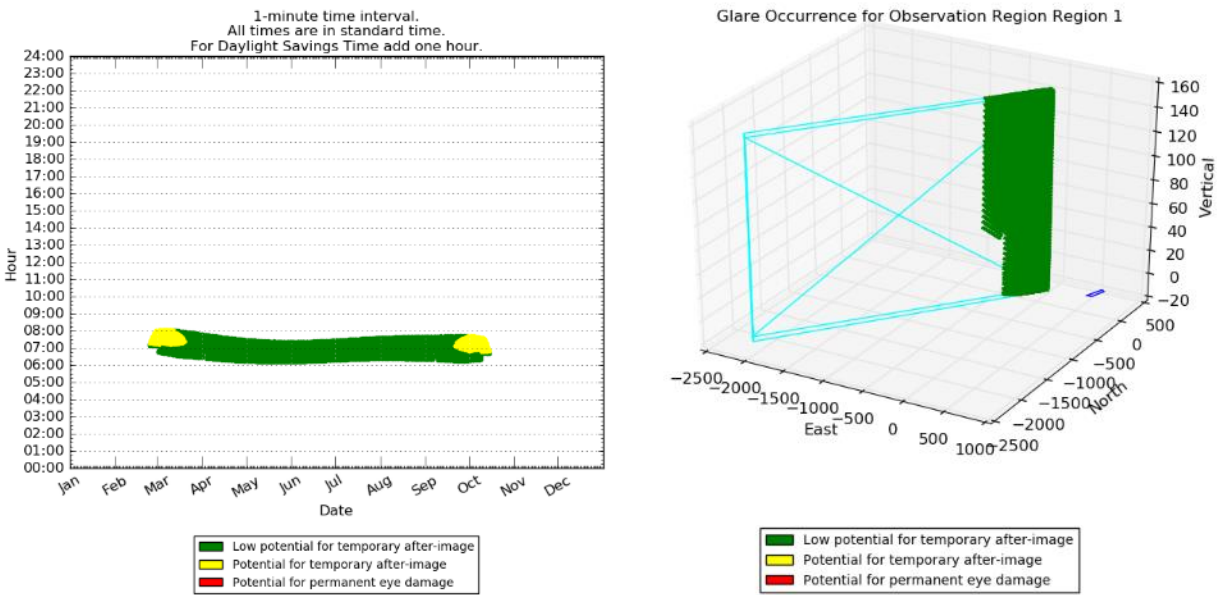


Figure 43. MHT block space analysis results. Occurrence plot (left) and spatial glare position plot (right) of block space region (light blue).

The parking garage PV array at MHT is often used as a baseline site due to its familiarity and well-known glare characteristics. For this trial, the original tilt and orientation values of 21 degrees and 200 degrees, respectively, were utilized. The OB was drawn over the western flight path, extending from 50 ft. above ground up to 600 ft.

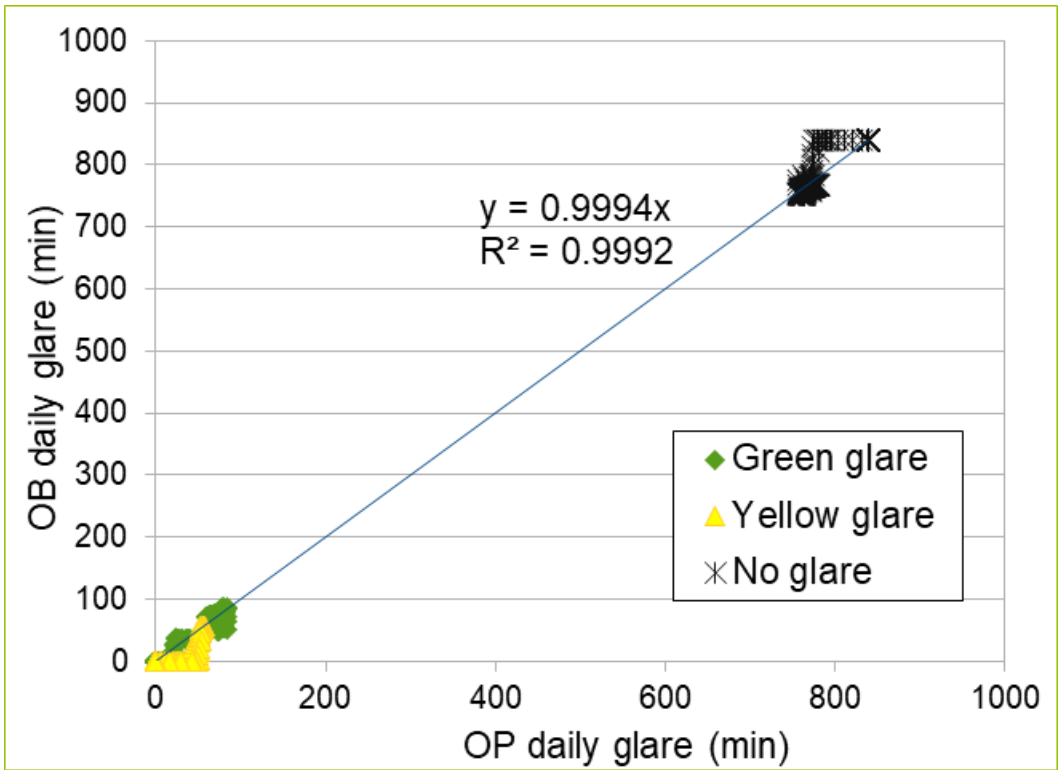


Figure 44. OB vs. OP daily unique glare for MHT.

The correlation coefficient for the OB vs. OP results at MHT was 0.9992.

Indianapolis International Airport

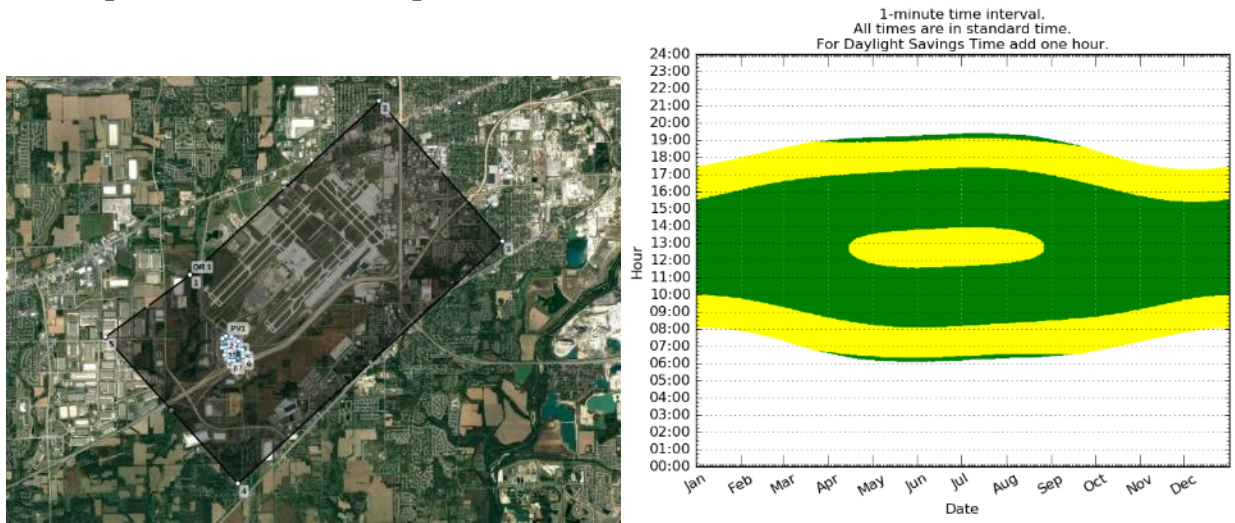


Figure 45. IND map editor display of PV array and encompassing block space (left). Glare analysis occurrence plot (right).

Indianapolis International Airport is an ideal location for validation. It is well-traveled, encompasses numerous parcels of land ideal for PV, and is well-known to the authors, who have

previously assisted with glare analyses there. Like MHT, this validation trial included one PV array and one OB. In this location, however, the OB included a substantial portion of airspace above the airport. A tilt of 15 degrees and orientation of 180 degrees were assumed for the PV array.

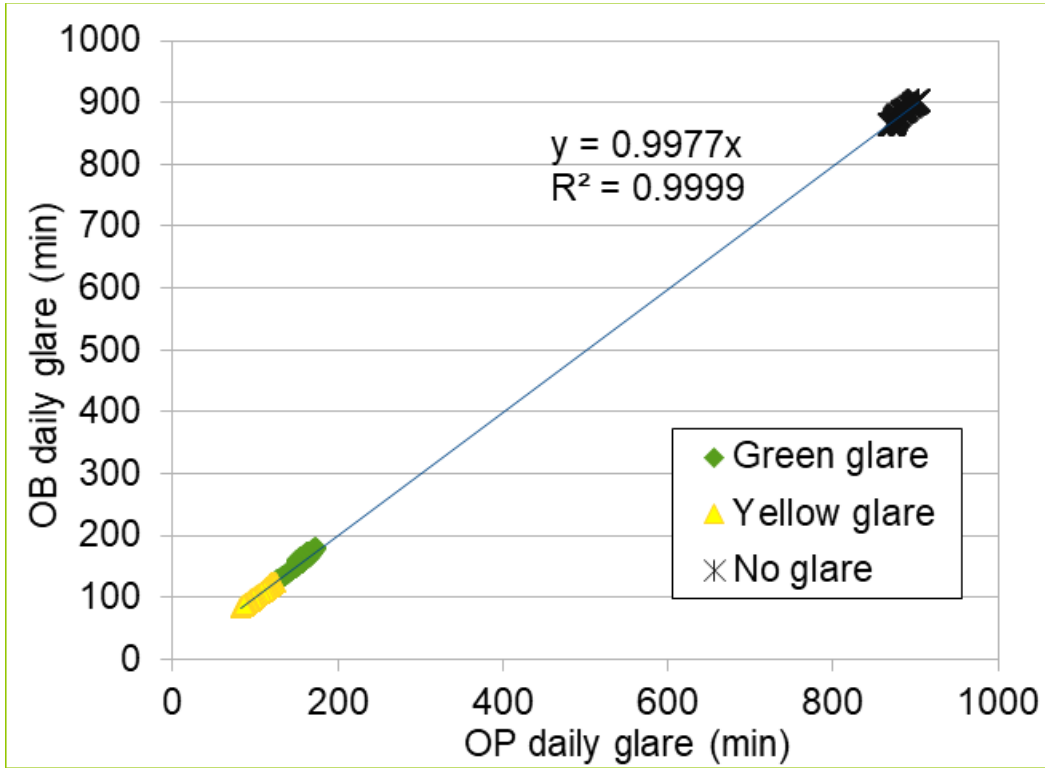


Figure 46. OB vs. OP daily unique glare for IND.

The validation process resulted in a correlation coefficient of 0.9999.

Cape Town International Airport (CPT)

CPT was utilized for the third block space validation. As with IND, the block space tool was used to model the airspace above the airport. A PV array with tilt of 20 degrees and orientation of 0 degrees (north) was introduced to validate the tool method for the southern hemisphere.



Figure 47 – Map editor illustrating CPT block space region and PV array to east.

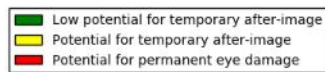
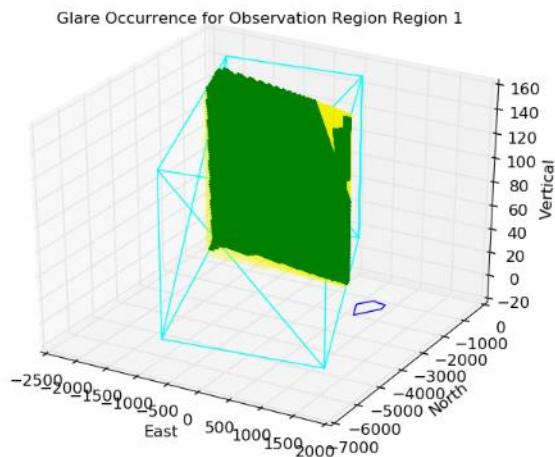
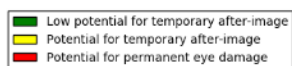
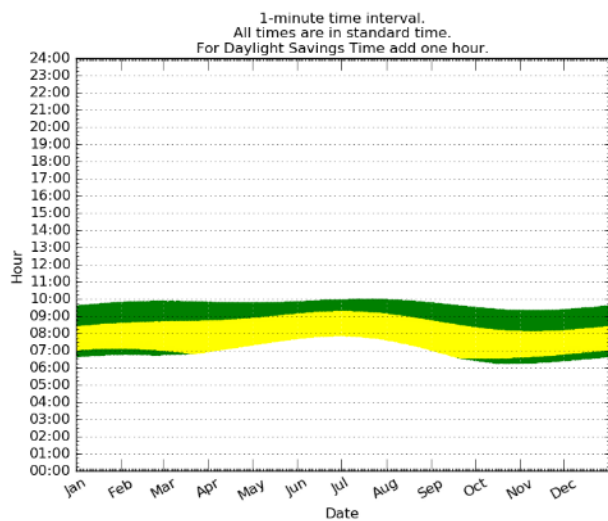


Figure 48. CPT block space analysis results. Occurrence plot (left) and spatial glare position plot (right) of block space region (light blue).

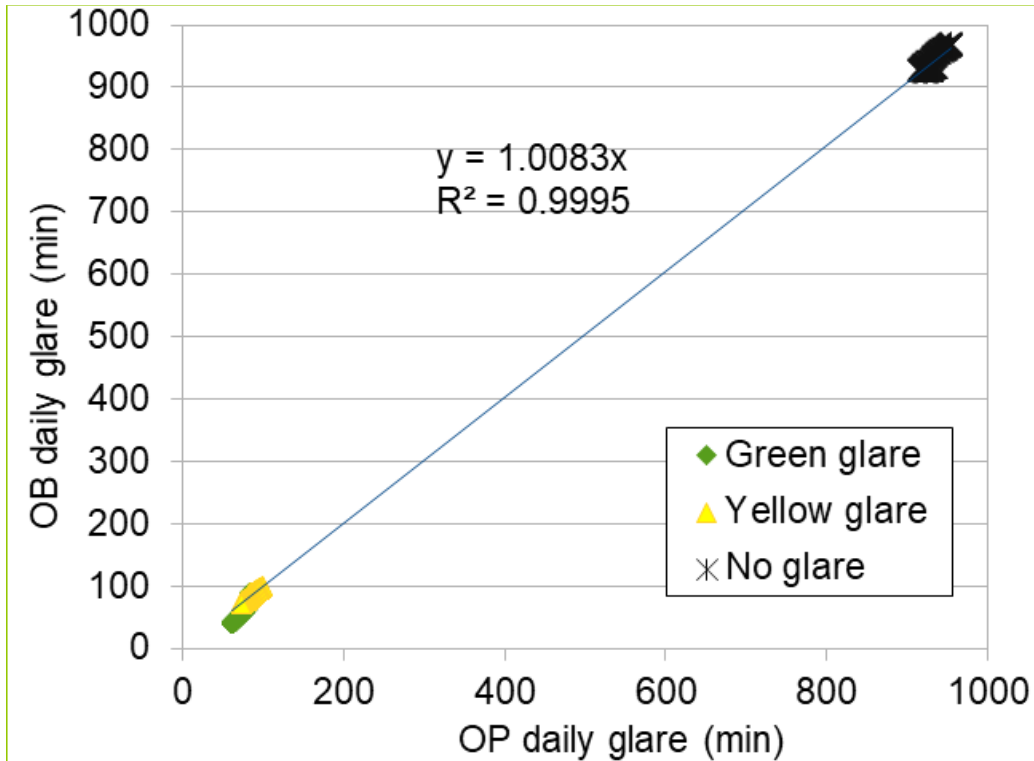


Figure 49. OB vs. OP daily unique glare for CPT.

The CPT correlation coefficient is 0.9995.

Summary

Three independent glare analysis trials were performed to validate the block space analysis feature. OB results were compared with results generated using the original Lookback method. In all three trials the correlation coefficient was > 0.99 , indicating successful validation.

DISTRIBUTION

All Electronic

1 Technical Library, 9536

sanddocs@sandia.gov



Sandia National Laboratories